

# N-BODY SIMULATIONS OF SATELLITE FORMATION AROUND GIANT PLANETS: ORIGIN OF ORBITAL CONFIGURATION OF THE GALILEAN MOONS

MASAHIRO OGIHARA

Nagoya University, Furo-cho, Chikusa-ku, Nagoya, Aichi 464-8602, Japan

AND

SHIGERU IDA

Tokyo Institute of Technology, Ookayama, Meguro-ku, Tokyo 152-8551, Japan

*Draft version May 24, 2018*

## ABSTRACT

As the number of discovered extrasolar planets has been increasing, diversity of planetary systems requires studies of new formation scenarios. It is important to study satellite formation in circumplanetary disks, which is often viewed as analogous to formation of rocky planets in protoplanetary disks. We investigated satellite formation from satellitesimals around giant planets through  $N$ -body simulations that include gravitational interactions with a circumplanetary gas disk. Our main aim is to reproduce the observable properties of the Galilean satellites around Jupiter through numerical simulations, as previous  $N$ -body simulations have not explained the origin of the resonant configuration. We performed accretion simulations based on the work of Sasaki et al. (2010), in which an inner cavity is added to the model of Canup & Ward (2002, 2006). We found that several satellites are formed and captured in mutual mean motion resonances outside the disk inner edge and are stable after rapid disk gas dissipation, which explains the characteristics of the Galilean satellites. In addition, owing to the existence of the disk edge, a radial compositional gradient of the Galilean satellites can also be reproduced. An additional objective of this study is to discuss orbital properties of formed satellites for a wide range of conditions by considering large uncertainties in model parameters. Through numerical experiments and semianalytical arguments, we determined that if the inner edge of a disk is introduced, a Galilean-like configuration in which several satellites are captured into a 2:1 resonance outside the disk inner cavity is almost universal. In fact, such a configuration is produced even for a massive disk  $\gtrsim 10^4 \text{ g cm}^{-2}$  and rapid type I migration. This result implies the inevitability of a Galilean satellite formation in addition to providing theoretical predictions for extrasolar satellites. That is, we can predict a substantial number of exomoon systems in the 2:1 mean motion resonance close to their host planets awaiting discovery.

*Subject headings:* planetary systems: formation – Planets and satellites: formation – Planet-disk interactions

## 1. INTRODUCTION

Origins of satellites around outer giant planets such as Jupiter and Saturn are important for determining the history of these objects, and their existence holds clues to the origins of such planets. Satellites around Jupiter and Saturn, in fact, are suitable targets for formation theories because their orbital parameters and compositions are well documented (e.g., Seidelmann 1992) compared to those of exoplanets. Therefore, we have developed a formation theory that compares physical parameters.

Besides satellites in the solar system, those in extrasolar systems, known as exomoons, are an additional focus of this study. Exomoons have recently attracted great interest because of their habitability. The number of detected extrasolar giant planets is much larger than rocky exoplanets, with the exception of Kepler candidates, and some orbit within the habitable zone (HZ), i.e., an orbital region in which the stellar flux is sufficient to maintain liquid water on the surface of a planet (e.g., Kasting et al. 1993). If rocky satellites orbit giant planets in the HZ, they are potentially habitable. According to studies on the possibility of life-bearing

moons (Williams et al. 1997, Kaltenegger 2000), satellites around extrasolar giant planets in the HZ might be habitable if their size is sufficient ( $\gtrsim 0.2 M_{\oplus}$ ). An obvious exception is Titan, which has a dense atmosphere even though its mass is  $\simeq 0.02 M_{\oplus}$ .

A detailed study on the detectability of habitable exomoons by Kipping et al. (2009) determined that exomoons in the HZ down to  $0.2 M_{\oplus}$  may be detected by transit timing effects, including transit timing variations and transit duration variations, with the expected performance of the *Kepler space telescope*. In fact, an ongoing observational project uses photometry data of *Kepler* to detect and investigate exomoon signals (Kipping et al. 2012). In addition, the possibility of screening the atmosphere of exomoons for habitability with transmission spectroscopy has been discussed by Kaltenegger (2010), who discovered that the number of transits needed to detect biomarkers on an Earth-like exomoon under idealized conditions and viewing geometry is feasible using the *James Webb Space Telescope (JWST)* for the sample of the closest M stars. Thus, it is important to predict the characteristics of satellites, such as mass, composition, and orbital location, that are likely to exist around extrasolar giant planets.

**Table 1**  
Properties of the Galilean Satellites

Satellites	$a$ ( $R_P$ )	$M$ ( $10^{-5} M_P$ )	$\rho$ ( $\text{g cm}^{-3}$ )	$e$	$i$ (rad)
Io	5.9	4.7	3.53	0.0041	0.0007
Europa	9.4	2.5	2.99	0.01	0.0082
Ganymede	15.0	7.8	1.94	0.0015	0.0034
Callisto	26.4	5.7	1.83	0.007	0.0049

**Note.** — Values are taken from Schubert et al. (2004) and Yoder (1995).  $a$ ,  $M$ ,  $\rho$ ,  $e$ , and  $i$  are the semimajor axis, mass, material density, eccentricity, and inclination of the satellites, respectively.

Regular satellites, which follow prograde and relatively close orbits up to tens of planetary radius with little orbital eccentricities and inclinations, are believed to have formed as by-products of planets' formation within a circumplanetary accretion disk (e.g., Lunine & Stevenson 1982). Circumplanetary disk models currently fall into two categories: (i) solids-enhanced minimum mass (SEMM) model (Mosqueira & Estrada 2003a,b; Estrada et al. 2009), in which a stationary disk is assumed; and (ii) gas-starved disk model (Canup & Ward 2002, 2006; Ward & Canup 2010), also known as a slow inflow disk, in which an actively supplied gaseous disk is considered.

In the SEMM model, a disk is composed of two different zones: an optically thick inner region with a peak surface density  $\sim 10^5 \text{ g cm}^{-2}$  and an optically thin outer region extended to a fraction of the Hill radius of the planet ( $\sim 0.2 r_H$ ). The transition from the inner disk to the outer disk is assumed to occur at the location between Ganymede and Callisto for the Jovian disk. In this model, the disk is static, that is there is no inflow from circumstellar orbits. The inner high density region with very low turbulent viscosity ( $\alpha \simeq 10^{-6} - 10^{-5}$ ) is practically inviscid. Solid components of the disk are supplied by ablation and capture of planetesimal fragments passing through the disk. In the gas-starved disk model, however, a low-mass viscously evolving disk with a peak surface density of  $\sim 100 \text{ g cm}^{-2}$  is considered. This disk is continuously supplied by the ongoing inflow of gas and dust particles from the protoplanetary disk. Disk conditions evolve in a quasi-steady state mode in response to the rate of gas accretion and turbulent diffusion, leading to lower disk gas densities than in the SEMM model. In this study, we adopt a fiducial model for gas surface density based on the gas starved disk model ( $\sim 100 \text{ g cm}^{-2}$ ). Note that if low disk viscosity or rapid gas inflow is assumed, the gas surface density can become higher than  $100 \text{ g cm}^{-2}$  (see Equations (3) and (4)).

Our main focus in this paper is the formation of Galilean-like satellites, although we extend our theory to exomoons and also comment on the Saturnian system later in this paper. Physical properties of the Galilean satellites are shown in Table 1. Orbital and compositional characteristics can provide valuable constraints on formation scenarios. The orbital resonances among the satellites Io, Europa, and Ganymede present a fascinating dynamic system. Io-Europa and Europa-Ganymede are in the 2:1 mean motion resonance, which causes their successive conjunctions to occur near the same longitude. These satellites are also in the Laplace resonance, which denotes the 1:1 commensurability between the rates of motion of the Io-Europa and Europa-Ganymede conjunc-

tions; thus, a triple conjunction never occurs. These resonances suggest that the Galilean satellites underwent orbital migration either during or after their formation. With regard to composition, a progressive increase in satellite ice mass fraction with increasing distance from Jupiter is observed. Io is composed of rock, and Europa, Ganymede, and Callisto are believed to contain approximately 8%, 45%, and 56% ice and water by mass, respectively (e.g., Schubert et al. 2004). In addition, Callisto's interior structure allows it to constrain its accretion timescale. Data from the *Galileo spacecraft* suggest that Callisto appears to be largely undifferentiated, provided that the satellite is in hydrostatic equilibrium (e.g., Anderson et al. 2001). Therefore, Callisto must have avoided melting in its entire history. Estimates of the temperature increase associated with accretional heating show that Callisto could have remained unmelted during formation if its accretion was on a timescale longer than  $5 \times 10^5$  years (Barr & Canup 2008). In addition, eccentricities and inclinations are considerably small, which are considered to be damped by the surrounding gas nebula and/or tidal dissipation within the satellites.

Formation of the Galilean satellites has been investigated from several perspectives. Canup & Ward (2006) performed  $N$ -body simulations of satellite accretion from satellitessimals in a starved disk that included the effects of a gas disk. Because the type I decay and accretion timescales are shorter than the disk lifetime, several generations of satellite formation and migration are repeated before gas disk dissipation. As the infall of gas and solid materials wanes because of global depletion of the circumstellar disk, the circumplanetary disk is depleted through viscous spreading and/or photoevaporation. Thus, the current satellites are the survivors of the final generation. Canup & Ward (2006) also found that the total satellite mass fraction to the host planet is regulated to  $\sim 10^{-4} M_P$  ( $M_P$ ; mass of the planet), which is only weakly dependent on model parameters and is consistent with Jovian and Saturnian systems.

Several authors attempt to clarify the origin of resonant states. Yoder (1979) and Yoder & Peale (1981) proposed that Io captured Europa into the 2:1 resonance through differential orbital expansion due to gravitational tides raised on Jupiter. With continuing orbital expansion, Europa eventually encountered the 2:1 mean motion commensurability with Ganymede, resulting in capture into the Laplace resonance. In contrast, Greenberg (1987) and Peale & Lee (2002) advocated a primordial origin of the resonant states through differential inward type I migration in the gaseous disk. Since the type I migration timescale is inversely proportional to the satellite mass, the largest satellite, Ganymede, underwent the most rapid drift and caught up with the inner satellites, leading to capture into the resonances. However, Canup & Ward (2006) performed detailed  $N$ -body simulations, which is the first  $N$ -body study of satellite accretion, and it is suggested that resonant states cannot be produced in their calculations<sup>1</sup>. It seems that the initial orbital configuration of Peale & Lee (2002) cannot

<sup>1</sup> Canup & Ward (2006) did not analyze whether the satellites evolved in resonances or not, but we performed  $N$ -body simulations under the same condition as Canup & Ward (2006) and confirmed that resonant relationships were hardly established.

be established during Canup & Ward’s  $N$ -body simulations, because when a Ganymede-mass satellite forms in outer region, satellites that reside in inner region do not grow to the mass comparable to those of Io and Europa.

As shown in recent studies on formation of close-in super-Earths (Terquem & Papaloizou 2007; Ogiwara & Ida 2009; Papaloizou & Terquem 2010), migrating bodies can be trapped in mean motion resonances near the disk inner edge. Sasaki et al. (2010) introduced the concept of the disk inner cavity in their investigation of satellite formation and found that four or five satellites are generally formed by being trapped in resonances, which agrees well with the Galilean satellites. Sasaki et al. (2010) adopted a semianalytical method rather than direct orbital integration and performed Monte Carlo simulations. Although this approach provides a powerful means for overall understanding of satellite formation, it is not adequate for effectively discussing detailed features of resonant trapping, because particularly in the formation of Galilean satellites, similar-sized satellites interact with each another, and multiple bodies are eventually trapped in resonances. Several studies outlined the prediction of capture probability for resonances as a function of initial particle eccentricity in the adiabatic limit, where the migration timescale is much longer than the resonant libration timescale (e.g., Murray & Dermott 1999). Recently, Quillen (2006) and Mustill & Wyatt (2011) studied a rapid migration case in the restricted three-body problem in the limit of low initial particle eccentricity and semianalytically obtained capture probability using a Hamiltonian model. However, it is uncertain whether their formulae can be used in a case in which bodies have comparable masses and the effect of eccentricity damping is included. Therefore, the  $N$ -body simulation is the only currently available method to accurately examine the detailed features of resonant trapping in systems in which multiple bodies with comparable masses interact with each other.

Thus, we conduct  $N$ -body simulations of satellite accretion in a gas-starved disk (Canup & Ward 2002) by adding an inner cavity to the original model, to clarify the formation scenario with the disk edge. In particular, we assess the probability of primordial formation of the resonance relationship. Moreover, we attempt to reproduce additional properties of Galilean satellites such as the total number and the compositional gradient.

Furthermore, we examine the dependence of model parameters on the properties of formed satellites. Recent studies on disk-planet interactions have suggested that torque exerted on a planet from a disk can be significantly altered because of disk structure (Masset et al. 2006) and radiative effects (e.g., Paardekooper et al. 2010), resulting in a discrepancy with the type I migration speed predicted by linear calculations (Tanaka et al. 2002). In an actively supplied disk, in which equilibrium between gas inflow and viscous diffusion is assumed, gas surface density depends on the inflow flux and gas viscosity. Given such uncertainties, we discuss satellite formation under a wide range of parameters. The results of this study are instrumental for effective prediction of orbital properties of extrasolar satellite systems.

In Section 2 of this paper, we detail our model and numerical method; in Section 3, we present the results of  $N$ -body simulations; in Section 4, we discuss the depen-

dence of model parameters on the properties of formed satellites; in Section 5, we briefly discuss satellite formation for the Saturnian system; and in Section 6, we summarize our conclusions and the implications of this study.

## 2. MODEL AND CALCULATION METHOD

Sasaki et al. (2010) considered two different models that correspond to Jovian and Saturnian systems: Surviving satellites around Jupiter were formed in a relatively massive protosatellite disk with an inner disk cavity, and those around Saturn were formed in a less massive and cooler disk without an inner disk cavity. These disk conditions are inferred from gap openings along the host planet’s orbit in the circumstellar protoplanetary disk and through observations of classical T-Tauri stars (CTTSs) and weak-line T-Tauri stars (WTTSs).

Gap openings require that both viscous and thermal conditions be satisfied (Lin & Papaloizou 1985). The critical masses are expressed as (Ida & Lin 2004):

$$M_{g,\text{vis}} \simeq 30 \left( \frac{\alpha}{10^{-3}} \right) \left( \frac{a}{1 \text{ AU}} \right)^{1/2} \left( \frac{M_*}{M_\odot} \right) M_\oplus, \quad (1)$$

$$M_{g,\text{th}} \simeq 120 \left( \frac{a}{1 \text{ AU}} \right)^{3/4} \left( \frac{M_*}{M_\odot} \right) M_\oplus, \quad (2)$$

where  $M_{g,\text{vis}}$  and  $M_{g,\text{th}}$  are the viscous and the thermal conditions, respectively. Although these masses have some uncertainties,  $M_{g,\text{vis}}$  and  $M_{g,\text{th}}$  are larger at Saturn’s orbits than at Jupiter’s orbit. Since Saturn’s mass is three times less than Jupiter’s one, it is plausible that Jupiter opened a gap to halt its growth while Saturn did not and Saturn’s growth was terminated by global dissipation of the solar nebula (Sasaki et al. 2010). As will be discussed in Section 2.1, gap openings lead to rapid depletion of protosatellite disks; satellites formed in a relatively massive protosatellite disk could survive around Jupiter, while those formed in a late-stage less massive disk could survive around Saturn.

Herbst & Mundt (2005) observed that spin periods of young stars show bimodal distribution in peaks at about 1 week and 1 day. They suggested that the stellar magnetic field of the 1-week-period stars is coupled with the circumstellar disk and is sufficiently strong to transfer spin angular momentum to the disk and open a disk inner cavity, whereas the disks around the 1-day-period stars do not have the cavity (see also Hartmann 2002). They also suggested that the 1-week and 1-day stars may correspond to CTTSs and WTTSs, respectively, enabling massive CTTS disks with a cavity to evolve to less massive WTTS disks without a cavity. In this evolution analogy, protosatellite disks may have a cavity in relatively early stages that disappears as the disk evolves, although this scenario includes a large uncertainty. Because the current spin rate of Jupiter is much slower than its break-up spin rate, magnetic coupling between Jupiter and the circum-Jovian disk is an obvious assumption. In fact, Takata & Stevenson (1996) showed that the circum-Jovian disk may have contained an inner cavity. The satellites formed in such a disk survived in case of Jupiter. The circum-Saturnian disk may once have contained a similar disk in early stages. However, if the disk evolved to a less massive disk without a cavity, the satellites formed in the massive disk would have fallen onto

Saturn, and the surviving satellites would have formed in the late-stage disk. We comment on the formation of the Saturnian system in Section 5. In the rest of this paper, we focus on the model for Jupiter.

### 2.1. Disk Model

#### 2.1.1. Gas Surface Density and Disk Temperature

As stated in Section 1, we adopted the actively supplied gas-starved disk model in our calculations. Our disk model is based on that by Sasaki et al. (2010), in which the disk inner cavity is added to the model by Canup & Ward (2002) with other slight modifications. In this section, we briefly summarize the model by Sasaki et al. (2010).

For the case in which gas inflow from the circumstellar disk is limited to the region between  $r_{\text{in}}$  and  $r_c$ , Canup & Ward (2009) suggested that the inner and outer radial boundaries of the inflow region for the proto-Jovian disk are  $4 R_J$  and  $34 R_J$ , respectively. This theory is consistent with the three-dimensional hydrodynamic simulation by Machida (2009), i.e.,  $r_c \sim 22 R_J$ , where  $R_J$  is the physical radius of Jupiter. As adopted by Canup & Ward (2006) and Sasaki et al. (2010), we used  $r_c = 30 R_P$  in this study. The total inflow rate is expressed as  $F_P = M_P/\tau_G$ , where  $\tau_G$  is the gas inflow timescale; then the infall flux per unit area is  $F_{\text{in}} = F_P/\pi(r_c^2 - r_{\text{in}}^2) \simeq F_P/\pi r_c^2$ . Here we ignore the radial dependence of the inflow because the resolution of the current hydrodynamic simulations is insufficient to constrain the radial dependence of the infall, as will be discussed in Section 5.

A disk is formed with the inflowing gas, which diffuses viscously. If the viscous diffusion timescale is shorter than the characteristic timescale over which the inflow changes, the gas disk can be described as a steady accretion disk, in which the inflow and viscous diffusion are equilibrated. According to the steady-state disk model derived by Canup & Ward (2002), the gas surface density of the disk is approximately given by (Appendix A)

$$\begin{aligned} \Sigma_g &\simeq 0.55 \frac{F_P}{3\pi\nu} \\ &\simeq 100 f_g \left(\frac{M_P}{M_J}\right) \left(\frac{r}{20R_P}\right)^{-3/4} \left(\frac{R_P}{R_J}\right)^{-3/4} \text{ g cm}^{-2} \quad (3) \\ f_g &\equiv \left(\frac{\alpha}{5 \times 10^{-3}}\right)^{-1} \left(\frac{\tau_G}{5 \times 10^6 \text{ yr}}\right)^{-3/4}, \quad (4) \end{aligned}$$

where  $\nu$ ,  $M$ ,  $r$ , and  $R$  are the viscosity, mass, radial distance from the planet, and physical radius of the bodies, respectively. The subscripts “P” and “J” denote quantities of the host planet and Jupiter, respectively. Because the magnitudes of turbulent viscosity and the gas inflow rate are not well determined, we introduce the scaling factor  $f_g$  for gas surface density. We adopt an alpha model for the disk viscosity (Shakura & Sunyaev 1973)  $\nu = \alpha c_s H \simeq \alpha c_s^2/\Omega_K$ , where  $H$  and  $\Omega_K$  are the disk scale height and the Keplerian angular velocity, respectively, and the sound velocity  $c_s$  is derived thorough the temperature distribution  $T$ .  $T$  is determined by the balance between viscous heating and blackbody radiation

(Appendix A) as follows:

$$\begin{aligned} T &\simeq 160 \left(\frac{M_P}{M_J}\right)^{1/2} \left(\frac{\tau_G}{5 \times 10^6 \text{ yr}}\right)^{-1/4} \\ &\times \left(\frac{r}{20R_P}\right)^{-3/4} \left(\frac{R_P}{R_J}\right)^{-3/4} \text{ K}. \quad (5) \end{aligned}$$

#### 2.1.2. Gas Dissipation and Disk Inner Edge

Gas surface density depends on the inflow rate; thus, the decay of the inflow leads to a decrease in gas surface density (and disk temperature). In our calculations, we generally assume an exponential decay of the inflow rate as  $F_P \times \exp(-t/\tau_{\text{dep}})$ , where the decay timescale  $\tau_{\text{dep}}$  is set to be  $10^6$  years. We therefore adopt an exponential decay of gas surface density with a dissipation timescale of  $10^6$  years. Although more accurate dependence of the inflow rate on the surface density is represented by  $\Sigma_g \propto F_P/\nu \propto F_P^{3/4}$ , we used the same decay timescale for simplicity.

Although infall flux decay associated with global dissipation of a protoplanetary disk is  $\sim 10^6$  years, we introduce a significantly more rapid decay associated with inflow truncation by the gap opening in the protoplanetary disk. After the gap opening, the protosatellite disk would be rapidly depleted on the viscous diffusion timescale  $\tau_{\text{diff}}$ ,

$$\tau_{\text{diff}} \sim \frac{r_c^2}{\alpha c_s^2/\Omega_K} \sim 10^3 \left(\frac{\alpha}{10^{-3}}\right)^{-1} \text{ yr}. \quad (6)$$

The gap opening timescale itself would be comparable to  $\tau_{\text{diff}}$  (Sasaki et al. 2010); therefore, both timescales are much shorter than accretion and migration timescales of satellites. In our calculations, the disk gas is abruptly dissipated with  $\tau_{\text{diff}}$ , such that the satellites are “frozen” at that time. Note that although hydrodynamic simulation suggests that the gap opening could not completely truncate the infalling gas (e.g., Lubow et al. 1999), even in this situation, results that are shown in this study remain unchanged because the infall rate would be reduced by several orders of magnitude. As long as the inflow cutoff timescale is shorter than accretion and migration timescales, which are  $\sim 10^5$  years, the results are not affected. That is, the results are not sensitive to the decay rate of the inflow.

As the location of the inner edge of the protosatellite disk is not well constrained, in our calculations, we set the disk inner edge at  $5 R_P$ , which is slightly outside the current corotation radius of Jupiter ( $\simeq 2.25 R_J$ ). At the disk inner edge, the gas surface density of the disk smoothly vanishes with a hyperbolic tangent function with the width  $\Delta r$ . We adopt  $\Delta r = 0.2 R_P$ , which is comparable to the disk scale height  $H$ . In addition, satellites that migrate inside  $4 R_P$  are disregarded from calculation mainly for computational reasons, which is also described in Section 2.4.2.

### 2.2. Solid Inflow Model

Based on the model used by Canup & Ward (2006), solid bodies are added to the calculation between  $r_{\text{in}} = 5 R_P$  and  $r_c = 30 R_P$  at a rate  $F_P \eta_{\text{ice}} f_{\text{d,in}}/100$ , where  $f_{\text{d,in}}$  and  $\eta_{\text{ice}}$  are the scaling factors of the amount of

**Table 2**  
Parameters for Each Simulation

Model (runs)	$f_g$	$f_{d,in}$	$C_I$	Ice Line
model 1(a,b,c)	1	1	1	No
model 2(a,b,c)	1	1	1	Yes
model 3(a,b,c)	10	1	1	No
model 4(a,b,c)	1	0.5	1	No
model 5(a,b,c)	1	2	1	No
model 6(a,b,c)	1	1	0.1	No
model 7(a,b,c)	1	1	10	No

**Note.** — Three runs referred to as a, b, and c (thus, a total of 21 runs) are performed for each model.  $f_g$  and  $f_{d,in}$  are scaling factors for gas surface density and the solid inflow, respectively.  $C_I$  is the scaling factor for the type I migration speed. For model 2, solid enhancement outside the ice line is considered.

solid material and the increase of solid materials due to ice condensation outside the “ice line,” respectively. The solid infall flux per unit surface area is assumed to be uniform because we assume a uniform infall flux of gas  $F_P$ , which is stated in Section 2.1.1. When  $\eta_{ice}f_{d,in} = 1$ , the gas-to-solid ratio in the inflow is assumed to be 100. However, the “effective” gas-to-solid ratio in the disk is not fixed to 100, because gas surface density is also parameterized by  $f_g$  and the solid materials which are decoupled from the gas evolve independently. (see Table 2 for the amount of gas of each run.) We assume an exponential decay of the solid inflow with the timescale of  $\tau_{dep}$ .

Although the infall of solid components is the continuous dust infall in the gas flow, it is mimicked by adding bodies with mass  $M_{add} = 5 \times 10^{-7} \eta_{ice}(r/15R_P)^3 M_P$  with a random azimuthal location at some time interval (see Supplementary Information in Canup & Ward 2006). Note that although a uniform solid inflow flux per area is assumed, radially dependent masses are used for adding bodies to avoid an imbalance in the number of adding bodies between radial zones. A total of 2,000–6,000 bodies are calculated for single runs, depending on the runs. The initial velocity dispersion of the proto-satellites is set to be their escape velocity. The corresponding initial eccentricity  $e$  and inclination  $i$  are given by  $v_{esc} = \sqrt{e^2 + i^2} v_K$  with  $e = 2i$  (Ida & Makino 1992).

In some runs, solid enhancement outside the ice line is adopted. Assuming the condensation temperature of  $\sim 160$  K, the location of the ice line is derived from Equation (5), and we consider that the ice line moves inward as the gas inflow rate decreases. Because  $T_d \propto F_P^{1/4}$  and  $T_d \propto r^{-3/4}$ , the location of the ice line is proportional to  $F_P^{1/3}$ :  $r_{ice} = 30 \exp(-t/3\tau_{dep}) R_P$ .

### 2.3. Orbital Integration

The orbits of satellitesimals are calculated by numerically integrating the equation of motion of the particle  $k$  at  $\mathbf{r}_k$  in planetocentric coordinates,

$$\begin{aligned} \frac{d^2 \mathbf{r}_k}{dt^2} = & -GM_P \frac{\mathbf{r}_k}{|\mathbf{r}_k|^3} - \sum_{j \neq k} GM_j \frac{\mathbf{r}_k - \mathbf{r}_j}{|\mathbf{r}_k - \mathbf{r}_j|^3} - \sum_j GM_j \frac{\mathbf{r}_j}{|\mathbf{r}_j|^3} \\ & + \mathbf{F}_{damp} + \mathbf{F}_{mig} + \mathbf{F}_{tide}, \end{aligned} \quad (7)$$

where  $k, j = 1, 2, \dots$ , the first term on the right-hand side is the gravitational force of the central planet, the second term is mutual gravity between the bodies, and the third is an indirect term.  $\mathbf{F}_{damp}$ ,  $\mathbf{F}_{mig}$ , and  $\mathbf{F}_{tide}$  are specific forces due to gravitational eccentricity damping, semimajor axis damping (type I migration), and tidal eccentricity damping, respectively, which will be explained in Section 2.4.

For numerical integration, we use the fourth-order Hermite scheme (Makino & Aarseth 1992) with a hierarchical individual time step (Makino 1991). When physical radii of two spherical bodies overlap, we consider the bodies to merge, conserving total mass and momentum and assuming perfect accretion. The physical radius of a body is determined by its mass  $M$  and internal density  $\rho$  as

$$R = \left( \frac{3}{4\pi} \frac{M}{\rho} \right)^{1/3}, \quad (8)$$

where we adopt  $\rho = 3 \text{ g cm}^{-3}$ .

### 2.4. Characteristic Timescales

#### 2.4.1. Gravitational Interaction with Disk Gas

We consider damping of orbital eccentricity, inclination, and semimajor axis due to disk-satellite interactions. A satellite gravitationally perturbs the disk gas and excites density waves, which damp  $e$ ,  $i$ , and  $a$  of the satellite<sup>2</sup> (e.g., Goldreich & Tremaine 1980; Ward 1986; Artymowicz 1993).

The force formulae for  $e$ -damping and  $i$ -damping ( $\mathbf{F}_{damp}$ ) are the same as that in Equations (2)-(4) in Ogihara et al. (2010), and the  $e$ -damping timescale is (Tanaka & Ward 2004)

$$\begin{aligned} t_e = -\frac{e}{\dot{e}} = & \frac{1}{0.78} \left( \frac{M}{M_P} \right)^{-1} \left( \frac{\Sigma_g r^2}{M_P} \right)^{-1} \left( \frac{c_s}{v_K} \right)^4 \Omega^{-1}, \quad (9) \\ = & 4.1 \times 10^3 f_g^{-1} \left( \frac{M}{10^{-4} M_P} \right)^{-1} \left( \frac{M_P}{M_J} \right)^{-3/2} \left( \frac{r}{20 R_P} \right)^{3/4} \\ & \times \left( \frac{R_P}{R_J} \right)^{3/4} \left( \frac{\tau_G}{5 \times 10^6 \text{ yr}} \right)^{-1/2} \text{ yr}. \end{aligned} \quad (10)$$

The force formula for  $a$ -damping ( $\mathbf{F}_{mig}$ ) is the same as that in Equation (3) in Ogihara et al. (2010), and the migration timescale is (Tanaka et al. 2002)

$$\begin{aligned} t_a = -\frac{a}{\dot{a}} = & \frac{1}{C_I} \frac{1}{2.7 + 1.1q} \left( \frac{M}{M_P} \right)^{-1} \left( \frac{\Sigma_g r^2}{M_P} \right)^{-1} \left( \frac{c_s}{v_K} \right)^2 \Omega^{-1}, \quad (11) \\ = & 1.2 \times 10^5 C_I^{-1} f_g^{-1} \left( \frac{M}{10^{-4} M_P} \right)^{-1} \left( \frac{M_P}{M_J} \right)^{-1} \left( \frac{r}{20 R_P} \right)^{1/2} \\ & \times \left( \frac{R_P}{R_J} \right)^{1/2} \left( \frac{\tau_G}{5 \times 10^6 \text{ yr}} \right)^{-1/4} \text{ yr}, \end{aligned} \quad (12)$$

where  $\Sigma_g \propto r^{-q}$  and  $q = 3/4$  is adopted from Equation (3).  $C_I$  is a scaling factor to allow for retardation

<sup>2</sup> This damping is sometimes called “tidal damping,” because damping of orbital elements through tidal energy dissipation within planets and tidal interactions between planets and satellites through their tidal deformation are also considered in this study, we use the term “tidal” only when we refer to the tidal energy dissipation in planets and the tidal interaction between planets and satellites.

and acceleration of type I migration. We include neither reverse torque of type I migration near the disk edge (Masset et al. 2006) nor the radiative effect through the entropy gradient (Paardekooper et al. 2010); such issues will be resolved in future studies. Instead, we handle  $t_a$  as a parameter in some runs and focus on the effect of the eccentricity trap, which is a physical mechanism to halt type I migration near the disk inner edge (Ogihara et al. 2010). This trapping arises when a body with an elliptical orbit straddles the disk inner edge; the body gains a net positive torque from the gas disk, which can compensate for negative type I migration torques that are exerted on a resonantly interacting convoy of bodies.

As discussed in Ogihara et al. (2010), Tanaka & Ward (2004) assumed small  $e$  and  $i$  ( $\ll c_s/v_K$ ) to obtain the damping rate of eccentricity. Ostriker (1999), Papaloizou & Larwood (2000), and Muto et al. (2011) showed that the formulae of  $e$ -damping and  $a$ -damping must be multiplied by correction factors in the case of supersonic flow. When the correction factors are added to  $t_e$  and  $t_a$ , it is suggested that the eccentricity trap becomes more efficient because the correction factor for  $t_a$  is a stronger function of  $ev_K/c_s$  than that for  $t_e$ . However, we neglect these factors for simplicity.

#### 2.4.2. Tidal Dissipation

Tidal dissipation within satellites plays an important role in satellite evolution. Thus, we incorporate tidal eccentricity damping of satellites as a force acting on them (Papaloizou & Terquem 2010):

$$\mathbf{F}_{\text{tide}} = -\frac{2}{t_{e,\text{tide}}} \frac{(\mathbf{v} \cdot \mathbf{r})\mathbf{r}}{|\mathbf{r}|^2}, \quad (13)$$

where the damping timescale is (Goldreich & Soter 1966)

$$t_{e,\text{tide}} = -\frac{e}{\dot{e}} = \frac{4}{63} \frac{M}{M_P} \left(\frac{a}{R}\right)^5 \tilde{\mu} Q \Omega^{-1} \quad (14)$$

$$\simeq \frac{4}{63} \left(\frac{M}{M_P}\right)^{-2/3} \left(\frac{a}{R_P}\right)^{13/2} \left(\frac{\rho}{\rho_P}\right)^{5/3} \tilde{\mu} Q \Omega^{-1} \quad (15)$$

$$\sim 10^9 \left(\frac{M}{10^{-4}M_P}\right)^{-2/3} \left(\frac{a}{20R_P}\right)^{13/2} \left(\frac{\tilde{\mu}Q}{1000}\right) \times \left(\frac{R_P}{R_J}\right)^{3/2} \left(\frac{M_P}{M_J}\right)^{-1/2} \text{ yr.} \quad (16)$$

Here,  $\tilde{\mu}$  ( $\simeq 3/2k_2$ ;  $k_2$  is the love number) and  $Q$  are the effective rigidity and the tidal dissipation function of the satellites, respectively. Although there is an uncertainty in  $Q$ , it is likely that both  $Q$  and  $\tilde{\mu}$  are of the order of 10-100 (Yoder 1995). We thus use  $Q' \equiv \tilde{\mu}Q = 1000$  for our  $N$ -body simulations.

Note that tidal torque on the satellite changes its semimajor axis. The migration timescale is (Goldreich & Soter 1966)

$$t_{a,\text{tide}} = \left|\frac{a}{\dot{a}}\right| = \frac{Q_P}{3k_{2,P}} \left(\frac{M}{M_P}\right)^{-1} \left(\frac{a}{R_P}\right)^5 \Omega^{-1} \quad (17)$$

$$\sim 10^{13} \left(\frac{Q_P}{10^5}\right) \left(\frac{k_{2,P}}{0.5}\right)^{-1} \left(\frac{M}{10^{-4}M_P}\right)^{-1}$$

$$\times \left(\frac{a}{20R_P}\right)^{13/2} \left(\frac{R_P}{R_J}\right)^{3/2} \left(\frac{M_P}{M_J}\right)^{-1/2} \text{ yr} \quad (18)$$

where  $Q_P$  and  $k_{2,P}$  are the tidal dissipation function and the love number of the central planet, respectively. The direction of migration is determined by the position of the satellite with respect to the corotation radius with the spin of the host planet. For example, if the satellite is on the inside of the corotation radius, the satellite moves inward. Because the migration timescale is generally much longer than the simulation time, we neglect this effect. The change in semimajor axis due to dissipation within the satellite is also ignored because this timescale is also long except for very close-in satellites. The migration timescale has a strong dependence on the semimajor axis; thus, extremely close satellites inside the corotation radius would fall onto the planet in a short time. As previously described, the current corotation radius of Jupiter is  $\simeq 2.25 R_P$ ; satellites that migrate inside of this radius would be quickly lost to the planet. Because of both computational cost and uncertainty in the corotation radius, we disregard bodies that reach  $4 R_P$  from our calculation.

### 3. TYPICAL RESULTS OF $N$ -BODY SIMULATIONS

In this section, we show typical results with our fiducial parameters; the parameters for each simulation are listed in Table 2. First, we perform  $N$ -body simulations in a gas disk that dissipates with the global dissipation timescale of  $\tau_{\text{dep}} = 10^6$  years, assuming that the solid inflow flux also decreases with the same timescale. Then, the host planet opens a gap in the circumstellar disk at a certain time to enable the gas and solid inflow fluxes to rapidly decrease with a disk viscous diffusion timescale of  $\tau_{\text{diff}} \sim 10^3$  years. However, because the timing cannot be determined, we randomly choose the moment and perform the subsequent simulation. We mainly focus on the  $N$ -body results in a gas disk because we found that orbital configurations do not change after rapid gas depletion.

#### 3.1. Growth and Migration before Gap Opening

Orbital evolution of satellites embedded in a gas disk is presented in this subsection. In our fiducial runs (models 1a, 1b, and 1c), the gas scaling factor  $f_g = 1$  is used, the solid inflow rate is fixed at  $f_{\text{d,in}} = 1$ , and the migration rate  $C_1 = 1$  is assumed to be that predicted by the linear theory. We note that these parameters are not unique values but contain some uncertainties. In Section 4, we will discuss the dependency of the results on these parameters. Other effects such as the supersonic correction factor of gravitational damping formulae and solid enhancement outside the ice line are not considered.

The orbital evolution for model 1a is shown in the bottom panel of Figure 1. In this figure, 30 most massive satellites at each time are plotted as circles, the radii of which are proportional to the radii of the bodies.  $T_K$  ( $\simeq 0.03$  years) is the orbital period at  $a = 20 R_J$  around a Jovian mass planet ( $M = M_J$ ). The dashed line at  $5 R_P$  represents the location of the disk inner edge. When a satellite with mass greater than  $10^{-5} M_P$  falls onto the host planet, it migrates inside  $4 R_P$ ; the descent is indicated by an arrow. The evolution of mass is shown in the top panel of Figure 1, which can be useful

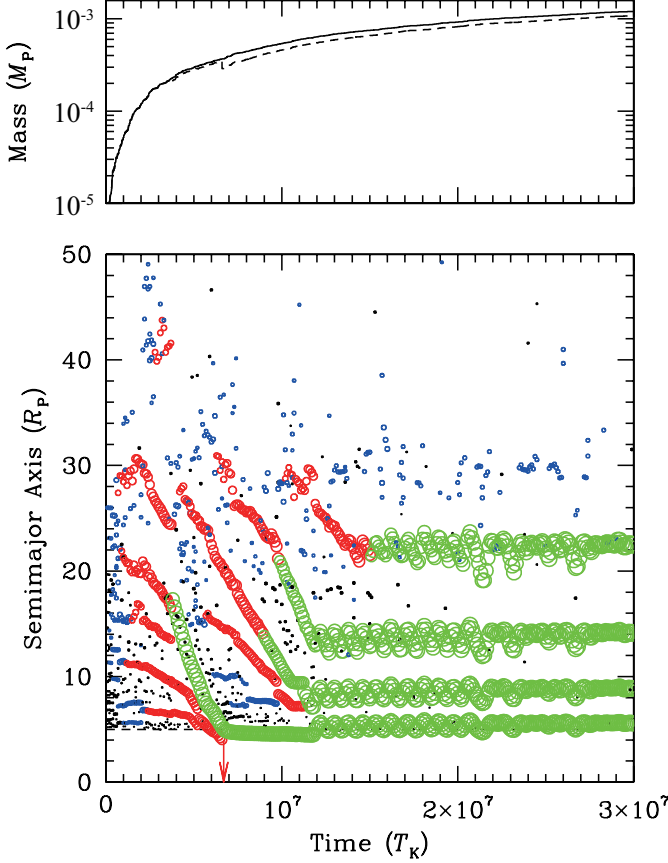


**Figure 1.** Top: Evolution of the solid mass for model 1a. The dashed line shows the total mass added to the calculation and the solid line shows the mass remaining within the disk. Bottom: Orbital evolution of the satellites for model 1a. For each time, 30 most massive satellites are plotted. The circles represent bodies, and the radii of the circles are proportional to the physical radii of the bodies. In the electronic version, bodies with  $M > 10^{-6} M_P$ ,  $M > 10^{-5} M_P$ , and  $M > 10^{-4} M_P$  are expressed with blue, red, and green circles, respectively. The arrow indicates that the satellite ( $\geq 10^{-5} M_P$ ) migrates inside  $4 R_P$ .

for physical understanding of what we observe here. The dashed line refers to the total mass added, and the solid line to the solid mass remaining within the disk.

Although many satellitessimals are not initially placed, solid materials are continuously added to the calculation, and the growth of satellitessimals proceeds in a manner similar to that of planetesimals around a star (e.g., Kokubo & Ida 1998). Through orbital repulsion of oligarchs that form from planetesimals, their orbital separations are kept wider than five mutual Hill radii. The typical orbital separation is  $\Delta r \simeq 10 - 15 r_H$ , where  $r_H$  is the mutual Hill radius of oligarchs. As is discussed in Canup & Ward (2006), it is important to note that owing to the low solid inflow rate, the growth rate of a satellite is governed by the solid inflow flux. The accretion timescale is given by

$$\tau_{\text{acc, inflow}} \simeq 1.8 \times 10^5 \eta_{\text{ice}}^{-1} f_{\text{d, in}}^{-1} \left( \frac{r}{20 R_P} \right)^{-2} \times \left( \frac{M}{10^{-4} M_P} \right)^{2/3} \text{ yr.} \quad (19)$$

More detailed descriptions of satellite growth and the

growth timescale are presented in Appendix B.

When the satellite grows to a critical mass, which is determined by a balance between the accretion time  $\tau_{\text{acc, inflow}}$  and migration time  $t_a$ , it begins to undergo orbital decay. The critical mass  $M_{\text{crit}}$  is estimated from Equations (12) and (19) as

$$M_{\text{crit}} \simeq 8 \times 10^{-5} \left( \frac{\eta_{\text{ice}} f_{\text{d, in}}}{C_1 f_g} \right)^{3/5} \left( \frac{M_P}{M_J} \right)^{-3/5} \left( \frac{r}{20 R_P} \right)^{3/2} \times \left( \frac{R_P}{R_J} \right)^{3/10} \left( \frac{\tau_G}{5 \times 10^6 \text{ yr}} \right)^{-3/20} M_P. \quad (20)$$

The critical mass in our fiducial case is  $\sim 8 \times 10^{-5} M_P$ , which is comparable to the masses of the Galilean satellites. Because satellites grow to some extent during migration, the factor  $(\eta_{\text{ice}} f_{\text{d, in}} / C_1 f_g)$  in Equation (20), which places a lower limit on the satellite mass, would be smaller than unity for the case of the Jovian satellite formation. A discussion of parameter dependence is given in Section 4.

The migrating satellites exhibit dynamics different from those in Canup & Ward (2006) because of the existence of the disk inner cavity. The satellite that reaches the disk inner edge no longer experiences gas drag, and migration ceases. The subsequently migrating satellite is captured into a 2:1 mean motion resonance with the inner satellite, leading to excitation of eccentricities ( $\simeq 0.1$ ) of both bodies. The inner satellite that resides near the disk inner edge gains a positive torque from the disk, and eventually, the satellites captured into the 2:1 mean motion resonance remain in the disk. This trapping mechanism of bodies near the disk edge has been both numerically and analytically investigated by Ogihara et al. (2010). They refer to the positive torque gained by the satellite and the trapping mechanism as the edge torque and the eccentricity trap, respectively. It should be emphasized that we do not establish a rigid wall at the disk inner edge or manually impose an edge torque to the satellite at the edge. We apply only instantaneous drag forces that have been physically examined in previous studies (Tanaka & Ward 2004) onto all bodies. If the body at the disk edge has a nonzero eccentricity, it moves back and forth between the inner cavity and the gas disk. When it moves into the gas disk near the apocenter, the tangential velocity of the body is slower than the local gas velocity; therefore, the body suffers a tailwind. On the other hand, when it enters into the cavity near the pericenter, where the tangential velocity of the body is faster than the local circular Keplerian velocity, the body does not feel gas drag, which results in a net positive torque on the body. Ogihara et al. (2010) determined that if the edge torque balances with the negative type I torque exerted on the bodies, the eccentricity trap works effectively and other migrating bodies can even be trapped without pushing the innermost body into the cavity. Figure 1 shows that the eccentricity trap is retained, except at  $t \simeq 7 \times 10^6 T_K$ . In fact, this trapping ordinarily also occurs in other simulations not shown here. However, an upper limit exists on the total number of satellites that can be retained in the disk, which is discussed in Section 4.2.

We also found that the 2:1 mean motion commensurability is universal in our  $N$ -body simulations. Figure 2



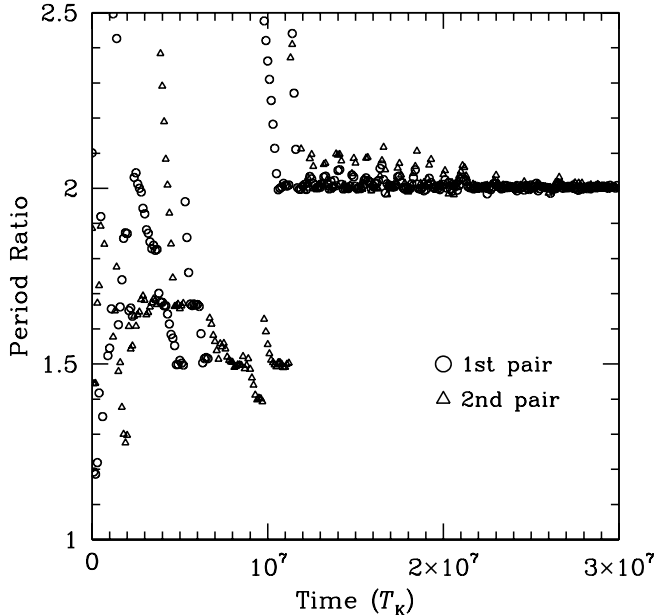


**Figure 2.** Evolution of the period ratios for model 1a. Circles and triangles express period ratios of the innermost and the second innermost pairs, respectively.

shows the evolution of period ratios. Open circles and triangles represent period ratios of the innermost and the second innermost pairs, respectively. Although some satellites are pushed inside the 2:1 resonant location by outer migrating satellites and are captured into closer first-order resonances (e.g., 3:2 and 4:3), almost all pairs, whose period ratios decrease above two, are locked in the 2:1 resonance. Hence, the period ratio is two. However, the resonant angles do not always librate about fixed values but sometimes exhibit circulation. The commensurate value and the occurrence of the eccentricity trap, which regulates the number of trapped bodies outside the disk edge, depends on eccentricity damping and migration rates, which is discussed in Section 4.

Satellites with mass  $M_{\text{crit}}$  begin to move inward and continue to grow during migration even after they are captured into a resonance. At  $3 \times 10^7 T_K$  when we stopped calculations, the masses were  $2.4 \times 10^{-4} M_P$  (innermost),  $2.5 \times 10^{-4} M_P$  (second innermost),  $2.9 \times 10^{-4} M_P$  (third innermost), and  $3.0 \times 10^{-4} M_P$  (fourth innermost), which are heavier than the current Galilean satellites. For satellites with masses comparable to those of the Galilean satellites to be formed, the gap opening time, in which the solid inflow is terminated, should be earlier than  $3 \times 10^7 T_K$ . In addition, the critical mass for migration (Equation (20)) must not exceed the masses of the Galilean satellites. A discussion of satellite mass appears in Section 4.3.

We performed two additional runs (models 1b and 1c) under the same conditions but with different random numbers for additional satellitesimal locations, and we confirmed that the overall evolutionary tendency is identical. The averaged orbital distributions of the four innermost satellites ( $\geq 10^{-5} M_P$ ) at each time are plotted in Figure 3. Circles, triangles, and squares represent averaged values over three simulations at  $1 \times 10^7$ ,  $1.5 \times 10^7$ ,

and  $2 \times 10^7 T_K$ , respectively. Error bars indicate  $1\sigma$  dispersion. The semimajor axis distributions that are obtained at given times are similar to those of the Galilean satellites. The three inner satellites are usually in the 2:1 resonance, and the fourth one is often captured into the 2:1 resonance. We set the disk inner edge at  $5 R_P$  so that the innermost one is located at  $5 R_P$ . This orbit is slightly interior compared with that of Io; thus, satellites in Figure 3 generally exist closer than the Galilean moons. The inclinations are kept small compared to the excited eccentricities due to resonant interactions, and they are comparable to the current inclinations of the Galilean satellites. Table 1 shows  $e$  and  $i$  of the Galilean satellites.

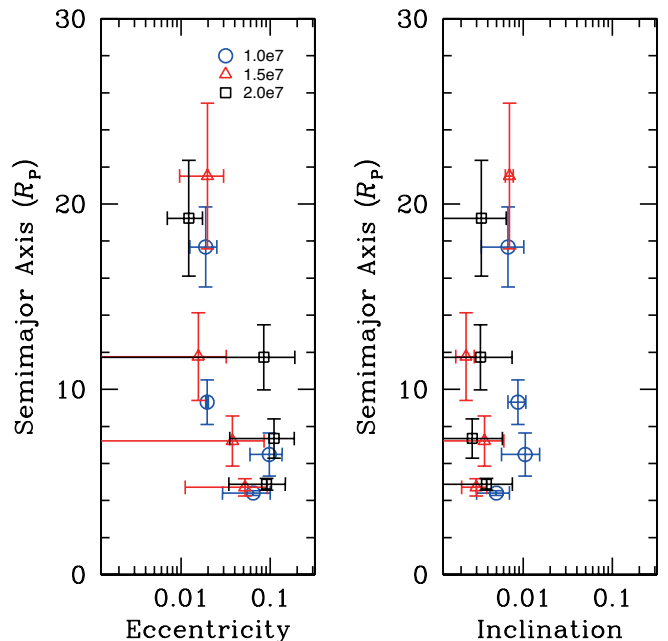


**Figure 3.** Averaged semimajor axes, eccentricities, and inclinations of the four innermost satellites at  $t = 1 \times 10^7 T_K$  (blue circles),  $t = 1.5 \times 10^7 T_K$  (red triangles), and  $t = 2 \times 10^7 T_K$  (black squares) for models 1a, 1b, and 1c, respectively. Error bars denote the  $1\sigma$  dispersion. (A color version of this figure is available in the online journal.)

### 3.2. Orbital Evolution after Gap Opening

The inflow is abruptly cut off because of the gap opening; thus, the disk gas is depleted at a certain time during the evolution in Figure 1. Because the time of the gap opening is unknown, we randomly choose the moment and continue calculations with gas dissipation on the timescale of  $\tau_{\text{diff}} = 10^3 \text{ years} \simeq 3 \times 10^4 T_K$ .

Figure 4 shows subsequent evolution of model 1a in which the orbital calculation is restarted at  $1.3 \times 10^7 T_K$ . Considering the formation of the Galilean moons in which the fourth satellite, Callisto, is not in a mean motion resonance, it is likely that this satellite underwent little or no migration. To achieve little significant migration, the gap opening timing, after which the circumplanetary disk dissipates on the timescale of  $\tau_{\text{diff}}$ , must be comparable to the timing of the completion of Callisto formation. We assume the time to be



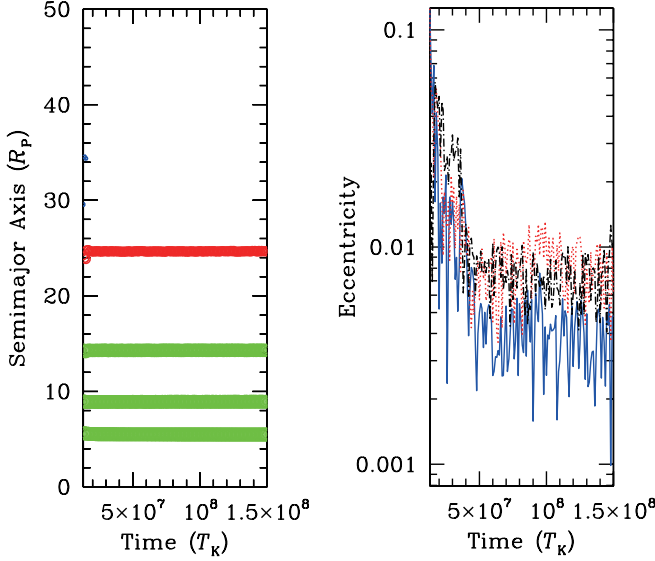


**Figure 4.** Subsequent evolution of model 1a with rapid gas dissipation. Left: Evolution of semimajor axis. Right: Evolution of eccentricities of the three inner satellites. The eccentricities of the innermost, the second innermost, and the third innermost satellites are expressed with the solid red line, the dotted blue line, and the dashed black line, respectively. (A color version of this figure is available in the online journal.)

$1.3 \times 10^7 T_K$ . An alternative scenario is that Callisto was accreted from the slowly inflowing materials during an imperfect gap opening (Sasaki et al. 2010), which naturally explains the inferred undifferentiated interior of Callisto (Barr & Canup 2008). Both scenarios explain the non-resonant Callisto. However, because the timing of gap opening cannot theoretically be predicted, more detailed discussion of characteristics of Callisto is left for future study.

The left panel of Figure 4 shows the semimajor axis evolution. Because the satellites are in mean motion resonances and their orbital separations are wide ( $\simeq 15 r_H$ ), orbital configurations hardly change. Although the semimajor axis can be slightly decreased because of tidal dissipation, such an effect is negligible. Tidal torque can also change the semimajor axis; however, we ignore this effect, as previously stated. The right panel shows the eccentricity evolutions of the innermost (solid line), the second innermost (dotted line), and third innermost (dashed line) satellites. The  $e$ -damping timescale of the innermost satellite, which is located at  $5 R_P$ , is estimated as  $\sim 10^6 T_K$  (Equation (16)). This result is not strictly consistent with the actual damping time ( $\sim 10^7 T_K$ ) of the innermost satellite observed in Figure 4, because eccentricities of outer satellites in resonances are also dragged down by tidal dissipation in the innermost satellite via resonant interactions between them. Thus, the eccentricities of the resonant satellites become  $\lesssim 0.01$ , which is consistent with those of the Galilean satellites (Table 1). Regarding the evolution of the resonant angles, as the orbital energy is dissipated because of tidal  $e$ -damping, the satellites evolve deeper into the resonances, leading to a small amplitude libration around  $0^\circ$  or  $180^\circ$ . Again, not all of resonant angles librate about fixed values. In three runs of all fifteen simulations (models 1, 3-6), the Laplace relationship, which indicates that  $\theta_5$  librates, can be ob-

served. The Galilean-like configuration ( $\theta_1, \theta_2, \theta_3$ , and  $\theta_5$  librate while  $\theta_4$  circulates) is reproduced by one run of all. The definition of the resonant angle is presented in Appendix C.

### 3.3. Origin of Compositional Gradient

By tracking the orbital evolution of all the satellites in the  $N$ -body simulation, satellite composition can be discussed. As mentioned in Section 1, a compositional gradient exists in the Galilean satellites. That is, bulk densities of Io, Europa, Ganymede, and Callisto are 3.53, 2.99, 1.94, and 1.83  $\text{g cm}^{-3}$ , respectively. The composition of satellites is considered to be a reflection of disk temperature; thus, we discuss in this subsection the origin of the compositional gradient in terms of disk temperature. Disks can be classified into three classes: (i) hot, in which only rocky materials exist; (ii) cool, in which the ice condensation line is located in the satellite-forming region, and rocky and icy objects coexist; (iii) cold, in which water vapor can condense into ice in all parts of the disk.

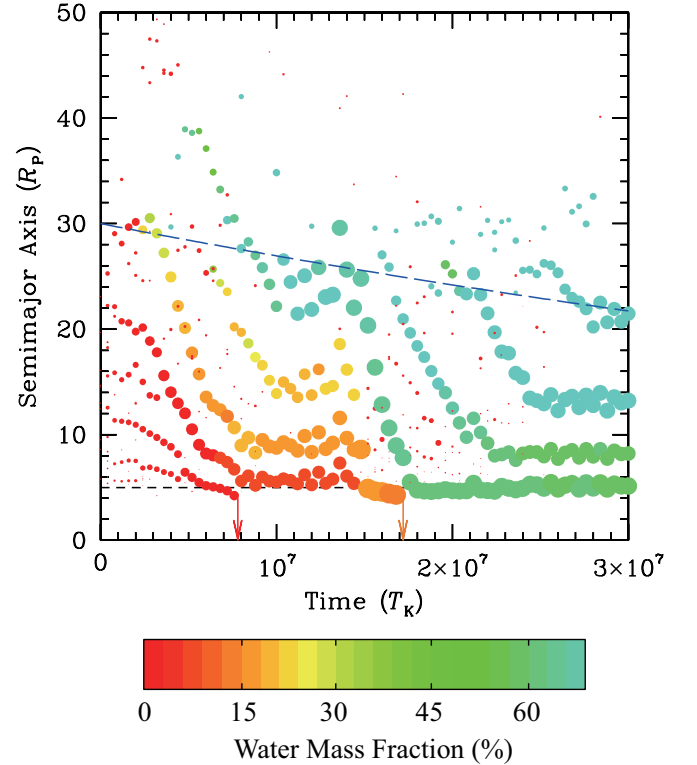


**Figure 5.** Evolution of semimajor axis and water mass fraction for model 2a. The color of each object corresponds to its water mass fraction. The long dashed line represents the location of the ice line  $r_{ice}$ .

To observe the effect of the ice line, we performed an additional set of  $N$ -body simulations (model 2) by considering the enhancement of solid materials outside the ice line assuming  $\eta_{ice} = 3$ , and we track the accumulation and migration of satellites. As noted in Section 2.2, we assume that the ice line moves inward according to  $r_{ice} = 30 \exp(-t/3\tau_{dep}) R_P$ , which indicates that a cool disk is considered. Figure 5 shows the evolution of model 2a, in which the colors correspond to the water (ice) mass fraction of satellites, from red (dry) to

light blue (up to 67%). (The colors are visible in the on-line version of the paper.) The long dashed line denotes the location of the ice line. The water content is calculated using the following prescription for components of satellites that originated at  $r$ :

$$\frac{M_{\text{water}}}{M} = \frac{\eta_{\text{ice}} - 1}{\eta_{\text{ice}}} \simeq \begin{cases} 0 & (r \leq r_{\text{ice}}) \\ 0.67 & (r > r_{\text{ice}}). \end{cases} \quad (21)$$

In the case without the disk inner edge, icy materials can reach the innermost region with the timescale of type I migration ( $\sim 10^6 T_K$ ), and fine-tuning of timing is required for the final survival of both rocky and icy satellites. The type I decay time should be comparable to the migration time of the ice line in the final state. However, as shown in Figure 5, icy satellites stay outer region ( $t = 1 - 1.5 \times 10^7 T_K$ ). Because satellites are lined up outside the disk inner edge, migrating icy satellitesimals are consumed by the outer satellites captured into mean motion resonances, leading to the deficiency of icy materials in the inner satellites. Thus, contamination of inner satellites by icy materials is prevented owing to the disk inner edge, and we do not have to rely on the fine-tuning of the timing. We find a monotonic increase in the water content with an increase in the distance from the planet. Between  $8 \times 10^6$  and  $1.5 \times 10^7 T_K$ , the water mass fraction of the innermost satellite is  $\simeq 5\%$ , while that of the outer satellite is  $\simeq 60\%$ . This configuration is approximately consistent with the those of Galilean satellites. However, after  $1.8 \times 10^7 T_K$ , the rocky inner satellites are lost to the planet because of the violation of the eccentricity trap. As a result, the surviving satellites contain a large quantity of ice ( $\gtrsim 40\%$ ).

Rather than the effect of the ice condensation line, we find in a companion paper (Nimmo, Ogihara & Ida, in preparation) that the impact erosion of ices during accretion can produce the compositional gradient even in a cold disk. We find that the impact velocity increases with a decrease in the radial distance and exceeds  $10 \text{ km s}^{-1}$  at the orbits of Io and Europa. This observation is attributed to the high Keplerian orbital velocity ( $\propto r^{-1/2}$ ) and a large velocity dispersion. Thus, nearly all ice in the innermost body, which corresponds to Io, and most of the ice in the second innermost body, which corresponds to Europa, evaporates through collisions. The amount of ice vaporization depends on the mass ratio of the target and the impactor, the impact velocity, and the impact angle (Kraus et al. 2011; Nimmo & Korycansky 2012). Detailed analysis is presented in the companion paper, in which the evaporation of ice owing to tidal heating is also discussed.

To summarize, to reproduce the compositional gradient by considering ice condensation outside the ice line, which indicates a cool disk, the following two conditions are necessary. First, the location of the ice line, in which there is an uncertainty, should be sufficiently far to enable the formation of a large amount of rocky satellitesimals. Second, once icy materials move into the inner satellite formation region, the eccentricity trap of a resonant convoy should not be broken. We also find that fine-tuning of timings is not required. It is suggested that the gap opening at which the satellites cease to form occurs during the period when satellites are trapped by the disk edge. This inferred gap opening time is consistent with

that assumed in Section 3.2. In addition, we find that even if satellites are formed in the cold disk, the origin of the compositional gradient can be explained by collisional erosion of volatiles, as discussed in the companion paper. Furthermore, we can exclude the possibility that the Galilean satellites are formed in the hot disk, that is, Jupiter did not open the gap in the protoplanetary disk when the circumplanetary disk was hot.

#### 4. DEPENDENCE ON PARAMETERS

In the previous section, we presented  $N$ -body results of satellite accretion for our fiducial parameters and reproduced the properties of the Galilean satellites (e.g., 2:1 commensurability). There are, however, uncertainties in the parameters that we used.

*Gas surface density ( $f_g$ ):* Following Canup & Ward (2006) and Sasaki et al. (2010), we assumed  $\alpha = 5 \times 10^{-3}$  and  $\tau_G = 5 \times 10^6$  years, leading to a gas-starved disk with  $f_g = 1$  (Equation (3)). This assumption of a small mass disk may be reasonable in the final stage of satellite formation because the inflow rate somehow decays, and gas surface density decreases. Recently, Fujii et al. (2011) suggested a low magnetic Reynolds number and thus a low turbulent viscosity, which may suggest a more massive disk ( $f_g > 1$  in Equation (3)).

*Amount of solid materials ( $f_{d,\text{in}}$ ):* We assumed  $f_{d,\text{in}} = 1$  for the amount of solid materials, in which the gas-to-dust ratio in the inflowing gas is considered to be 100 according to solar metallicity. It is inferred that “metal” abundance in Jupiter is high (e.g., Saumon & Guillot 2004); thus, the inflowing gas would be more metal-rich (thus  $f_{d,\text{in}} > 1$ ). This could be due to depletion of local gas by accretion onto Jupiter or that toward the Sun, leaving an excess of solid materials. However, dust grain abundance may also be reduced due to solids having been incorporated into planetesimals, which decreases  $f_{d,\text{in}}$ . Thus, depending on which effect is dominated,  $f_{d,\text{in}}$  can be larger or smaller than unity.

*Efficiency of type I migration ( $C_1$ ):* In the fiducial model, the type I migration speed is set to the value derived from the linear calculation ( $C_1 = 1$ ). Several mechanisms for reducing migration efficiency have been discussed (e.g., Masset et al. 2006; Paardekooper et al. 2010). In fact, to reproduce the observed distributions of exoplanets,  $C_1 \lesssim 0.1$  (Ida & Lin 2008).

In this section, therefore, we first examine the mechanism through which the  $N$ -body results are altered by adopting different parameter values, and we attempt to link the model parameters to the physical properties of formed satellites, such as the resonant relationship, by using semianalytical arguments. This approach, in which

dependences of parameters on properties of satellites are investigated, is valid not only for setting limits on parameters that reproduce the Galilean satellites but also for discussing satellite formation in general, including satellite formation around extrasolar giant planets.

#### 4.1. *N*-body Simulations with Various Parameters

We present the results of *N*-body simulations with various parameters in Figures 6(a)-(e). The model parameters for each simulation are summarized in Table 2. The left panels of Figures 6 show orbital evolution of each representative run, while the right panels display averaged orbital distributions of the four innermost satellites at each time over three runs. An exception is Figure 6(e) in which only the three innermost satellites are plotted. The times are selected after the time at which the innermost satellite reaches the disk inner edge.

Figure 6(a) shows the case of model 3, in which the gas surface density is 10 times higher than that adopted in model 1. Although the damping timescales of the eccentricity and the semimajor axis due to the gravitational drag become 10 times shorter, the trend agrees with that of model 1. Three to five satellites are lined up outside the disk inner edge, and they generally exhibit 2:1 mean motion commensurabilities. The critical mass for starting migration drops to  $\simeq 2 \times 10^{-5} M_P$ , and the masses of satellites trapped near the edge are comparable to those of the Galilean satellites ( $\simeq 5 \times 10^{-5} M_P$ ) before  $t = 6 \times 10^6 T_K$ . After this time, the masses continue to increase as the satellites accrete inflowing solid materials. At  $t = 3 \times 10^7 T_K$ , the mass of the satellites that are trapped by the edge become  $\simeq 3 \times 10^{-4} M_P$ , which is consistent with model 1 because the solid inflow rate is the same as that of model 1 ( $f_{d,in} = 1$ ). Despite the increase in the eccentricity damping force, the eccentricities of the satellites captured into resonances are nearly comparable to those in model 1, because the eccentricities of the satellites exhibiting the eccentricity trap are given as a function of  $t_e/t_a$  (Ogihara et al. 2010).

Figures 6(b) and (c) show the results of models 4 and 5, respectively, in which the inflow rate of solid materials is changed. The critical mass for migration is proportional to  $f_{d,in}^{3/5}$ ; thus, the change of the inflow rate by a factor of 2 leads to a variation of the critical mass by a factor of  $2^{3/5}$ . The masses of satellites that are trapped by the edge at  $3 \times 10^7 T_K$  are  $\simeq 1.5 \times 10^{-4} M_P$  (model 4) and  $\simeq 6 \times 10^{-4} M_P$  (model 5). Although the masses of the migrating satellites change, altering the migration rate, the overall results are hardly affected. In particular, three to four satellites are captured into the 2:1 mean-motion resonance as is found in the fiducial model.

Figures 6(d) and (e) show the results of models 6 and 7, in which the type I migration speed is reduced (model 6) and increased (model 7) from model 1 by a factor of 10. The critical mass is changes; however, the orbital configuration in model 6, in which approximately four satellites in the 2:1 resonance are trapped by the edge, is approximately the same as in model 1. The masses of satellites trapped by the edge at  $3 \times 10^7 T_K$  are also comparable to those in model 1. However, the eccentricity trap is no longer effective in model 7, which results in orbital distributions of satellites that differ significantly from those in other models.

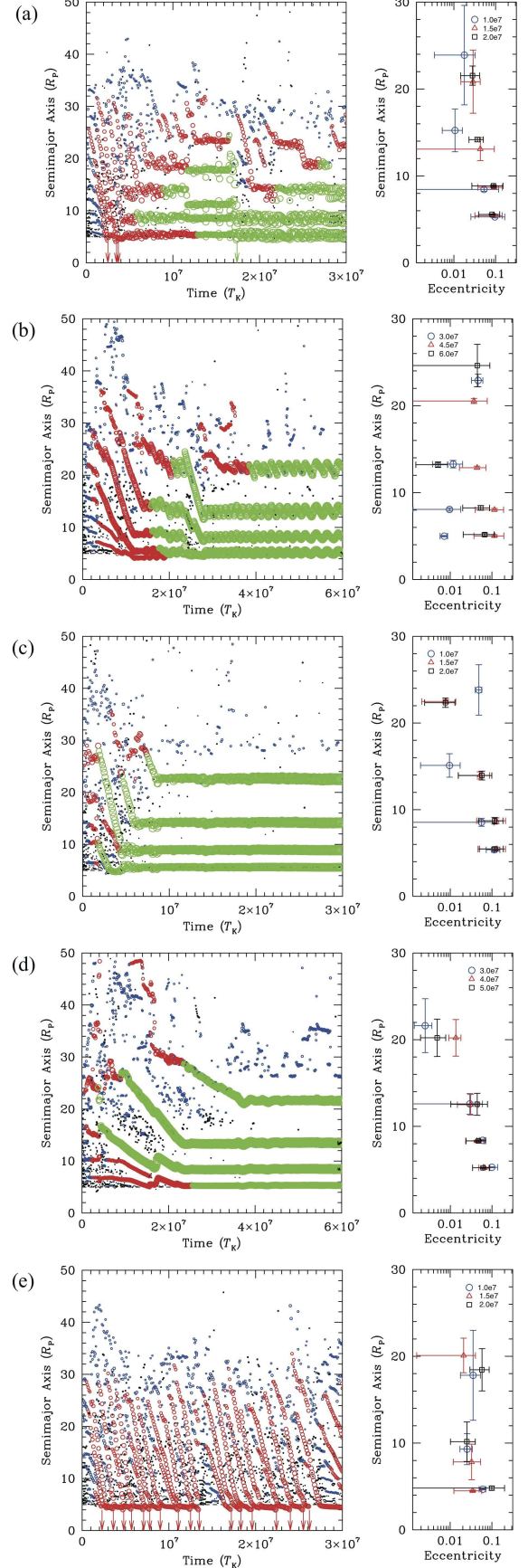


**Figure 6.** Results of *N*-body simulations of (a) model 3, (b) model 4, (c) model 5, (d) model 6, and (e) model 7. Left: Same as that described in Figure 1, with orbital evolution for representative runs. Right: Same as that described in Figure 3, with averaged orbital distributions.

#### 4.2. Resonances and Number of Satellites

In this subsection, we discuss properties of remaining satellites in detail. To further discuss the resonant configuration and the total number of formed satellites over a wide parameter range, we calculate the orbital evolution of hypothetical three satellite systems. Here we show that capture into 2:1 resonance is robust for a reasonable range of parameters. The masses of satellites are set to  $10^{-4} M_{\text{P}}$ . The gas surface density  $f_{\text{g}}$ , which affects damping rates of  $e$  and  $a$ , and the migration speed  $C_1$  (hence  $t_e/t_a$ ) are treated as free parameters. The results are summarized in Figure 7. Filled circles and filled squares in the figure indicate that all the three satellites exhibit the eccentricity trap and are captured into the 2:1 and 3:2 resonances, respectively. Filled triangles represent the cases in which the satellites exhibit the eccentricity trap but the inner pairs are in the 2:1 resonance and the outer pairs are in the 3:2 resonances. Inverted triangles represent inner pairs in the 3:2 resonance and outer pairs in the 2:1 resonances. Open squares represent transitional cases from the filled triangles to the filled squares in which inner and outer pairs are temporarily captured into the 2:1 and 3:2 resonances, respectively, outside the disk edge; after a while, configurations of the inner pairs are converted to the 3:2 resonance when the innermost satellites move inside the edge. Crosses represent cases in which the eccentricity trap is not realized, although the satellites are captured into the 2:1 or 3:2 resonances. Asterisks show cases of satellites collisions.

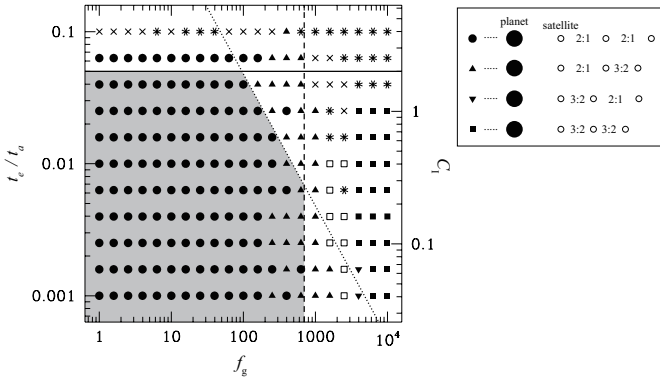


**Figure 7.** Results of three body calculations for various values of  $f_{\text{g}}$  and  $t_e/t_a$ . Filled circles indicate that all three satellites are captured into the 2:1 resonance outside the disk inner edge. Solid, dashed, and dotted lines represent semianalytically estimated limits by Equations (24), (31), and (32), respectively.

We find that the region (filled circles) in which satellites are captured into the 2:1 resonance outside the disk edge is vast. In fact, even with rapid migration ( $C_1 \simeq 2.5$ ) and a high gas surface density ( $f_{\text{g}} \simeq 10^2$ ;  $\Sigma_{\text{g}} \simeq 10^4 \text{ g cm}^{-2}$ ), final configurations are identical. This region represents the necessary condition for the formation of the Galilean satellites, suggesting that a Galilean-like configuration in which the three satellites are in the 2:1 mean motion resonance can be formed with near certainty if the disk inner edge is sufficiently sharp. In some runs, we observe that the Laplace angle  $\theta_5$  librates about some fixed values.

It is difficult to derive analytical formulae that represent the filled circle region because resonant capture

for equal-mass multiple systems has not been analytically discussed. Therefore, we obtain semianalytical conditions by using simplified treatments. From Figure 7, we find that the following three conditions are necessary for capture into the 2:1 resonance outside the disk edge: (i) satellites should be trapped owing to the eccentricity trap to avoid falling onto the planet, (ii) eccentricity damping should not be excessively strong, and (iii) the migration speed should not be extremely rapid. Next we derive semianalytical formulae for each condition.

Initially, the condition (i) is considered. For the eccentricity trap to occur, a constraint on  $t_e/t_a$  (hence  $C_1$ ) is derived by an argument similar to that provided in Ogihara et al. (2010). If the edge torque, which is exerted on the innermost satellite because of the eccentricity damping force, balances migration torques of the outer satellites, then the satellites can be trapped by the edge. The trapping condition is obtained from Equation (32) of Ogihara et al. (2010):

$$\frac{-A_{\theta}^c}{0.78} \frac{e}{\pi} \frac{1}{t_e} - \frac{1}{2t_a} - \frac{n-1}{2t_a} > 0, \quad (22)$$

where  $A_{\theta}^c (= -0.868)$  is the numerical coefficient (Tanaka & Ward 2004),  $e$  is the eccentricity of the innermost satellite, and  $n$  is the number of trapped satellites. The first term is the edge torque, the second term is the migration torque on the innermost satellite, and the third term is the resonant torque from outer satellites. Here, we assume that the satellites have nearly equal masses for simplicity. (Note that we used a more accurate expression for the edge torque than that in Equation (32) of Ogihara et al. (2010).)

From numerical calculations, eccentricities excited by resonances are well fitted by

$$e \simeq 0.6 \left( \frac{t_e}{t_a} \right)^{1/2} \left( \frac{n}{3} \right)^{1/2}. \quad (23)$$

Substituting Equation (23) into Equation (22), the following constraint on  $t_e/t_a$  is obtained:

$$\frac{t_e}{t_a} < 0.05 \left( \frac{n}{3} \right) \left( \frac{2}{n-1} \right)^2, \quad (24)$$

where the second term of Equation (22) is ignored. The orbit of the innermost satellite partially enters the inner cavity, in which the satellite is not affected by the type I torque. In this case, the magnitude of type I migration torque on the innermost satellite should be smaller than  $1/2t_a$ , and the third term dominates the second term (Ogihara et al. 2010). The capture constraint by the eccentricity trap is plotted with a solid line in Figure 7. This condition is consistent with the results of orbital calculations.

Then, from condition (ii), we derive a constraint by comparing timescales of excitation and eccentricity damping. The eccentricity excitation by a single distant encounter of two satellites on approximately circular orbits is given by (Hasegawa & Nakazawa 1990)

$$\delta e \simeq 6.7 \left( \frac{b}{r_{\text{H}}} \right)^{-2} \left( \frac{r}{r_{\text{H}}} \right)^{-1}, \quad (25)$$

where  $b$  is the difference in the semimajor axes of the two satellites. Because the distant encounter occurs at every



synodic period

$$T_{\text{syn}} \simeq \frac{2\pi r}{3b\Omega/2}, \quad (26)$$

the variation of eccentricity per unit time is expressed as

$$\left. \frac{de}{dt} \right|_{\text{scat}} \simeq \frac{\delta e}{T_{\text{syn}}} \simeq 10 \left( \frac{b}{r_H} \right)^{-1} \left( \frac{r}{r_H} \right)^{-2} \frac{\Omega}{2\pi}. \quad (27)$$

For first-order resonances of  $j : j - 1$ , the orbital separation is expressed as

$$b = \left[ \left( \frac{j}{j-1} \right)^{2/3} - 1 \right] a, \quad (28)$$

then, Equation (27) is reduced to

$$\left. \frac{de}{dt} \right|_{\text{scat}} \simeq 1.7 \times 10^{-2} \left( \frac{M}{10^{-4} M_P} \right) \left( \frac{r}{20R_P} \right)^{-3/2} \times \left( \frac{R_P}{R_J} \right)^{-3/2} \text{yr}^{-1}, \quad (29)$$

where  $j = 2$  is assumed in the final transformation. A necessary condition for capture into a resonance is that  $e$ -excitation due to distant encounters should be larger than  $e$ -damping due to the gas drag described in Equation (10):

$$\left. \frac{de}{dt} \right|_{\text{scat}} > \frac{e}{t_e}. \quad (30)$$

This leads to the following constraint on  $f_g$ :

$$f_g < \frac{70}{e} \left( \frac{M_P}{M_J} \right)^{-3/2} \left( \frac{r}{20R_P} \right)^{-3/4} \left( \frac{R_P}{R_J} \right)^{-3/4} \times \left( \frac{\tau_G}{5 \times 10^6 \text{yr}} \right)^{-1/2}. \quad (31)$$

From Figure 7, we find that the capture condition for the 2:1 resonance is well explained by  $f_g < 700$ , in which  $e \simeq 0.1$  is used. This capture constraint is plotted with a dashed line in Figure 7.

Finally, from condition (iii), a necessary constraint condition on the migration speed is derived. According to both analytical (Friedland 2001) and numerical (Ida et al. 2000; Wyatt 2003) studies of resonant trapping, capture probability depends on the mass and the semimajor axis. The dependence of the critical migration rate, which can be represented by  $C_{1,\text{crit}}$ , for trapping is given as  $C_{1,\text{crit}} \propto (M/M_P)^{-4/3} \Omega^{-1}$ . Then, we adjust the coefficient by our numerical calculations. The numerical result shown in Figure 7 is fitted as

$$C_1 < 200 f_g^{-1} \left( \frac{M}{10^{-4} M_P} \right)^{-4/3}, \quad (32)$$

which is the critical migration timescale of the three satellites for the 2:1 resonance, and it is plotted with a dotted line in Figure 7.

The enclosed shaded region in Figure 7 represents the condition for formation of Galilean-like satellites. The results of three satellite calculations and the semi-analytical arguments are consistent with the results of  $N$ -body simulations. Figure 8 indicates the parameters

used in our  $N$ -body simulations on the gas surface density ( $f_g$ ) and the migration speed ( $C_1$ ) plane. The shaded region corresponds to that in Figure 7. In case of models 1-6, the parameters are in a good region for reproducing the number and the resonant relationships of the Galilean satellites, while the parameter values of model 7 is far from the eccentricity trapping limit.

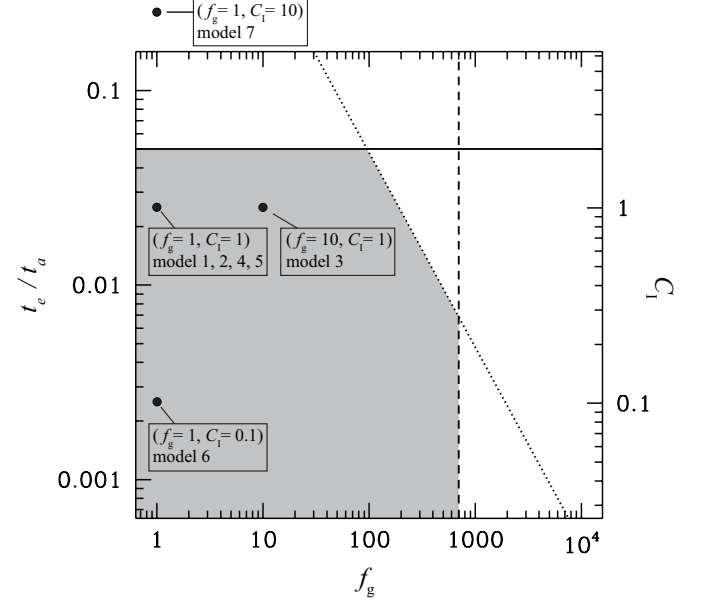


**Figure 8.** Model parameters adopted in  $N$ -body simulations. The parameters of model 7 are outside the shaded region, which are derived by a semianalytical argument.

We also compare our results with previous studies, in which the Hamiltonian model is used in case of rapid migration (Quillen 2006; Mustill & Wyatt 2011). These studies have considered the circular restricted three-body problem with a massive planet and a massless test particle orbiting a central star to derive capture probability for first- and second-order resonances. Because the bodies with comparable masses are captured into resonances in our simulation and the effect of eccentricity damping is included, it is not possible to directly apply their predictions to our case. However, we find that their results are approximately consistent with our  $N$ -body results and hence our semianalytical arguments. In Mustill & Wyatt (2011), capture probability is derived as a function of the generalized momentum  $J$  and the migration rate  $\dot{\beta}$ . Since  $J \sim 10^{-1}$  and  $\dot{\beta} \sim 10^{-2}$  are derived in the case of model 1, it is determined from Figures 2 and 11 in Mustill & Wyatt (2011) that capture into the 2:1 resonance is highly likely. Therefore, our findings of a robust 2:1 resonance formation are also confirmed by the Hamiltonian model. In addition, Mustill & Wyatt (2011) documented the following trends, which is also observed in our calculations: capture probability decreases with a decrease in mass. If the migration rate increases by  $10^3$  times of that in model 1, bodies tend to be captured into the closer 3:2 resonance. These features therefore agree with our semianalytical estimates. Further investigation of the resonant capture for comparable masses including eccentricity damping is expected in future work.

Finally, we note that since the satellites are captured

into the 2:1 resonance, the orbital difference  $b$  is generally  $\simeq 10 - 15 r_H$ , which is larger than  $b = 5 r_H$  assumed in Sasaki et al. (2010). In their calculations, small satellites are trapped between large satellites; as a result, orbital differences between large satellites become  $\sim 15 r_H$ . Their assumption is valid for relatively fast migration cases (e.g., planet formation); therefore slight improvement is needed. This is also discussed in Section 5.

#### 4.3. Mass

In this subsection, we discuss the satellite mass by using semianalytical estimates. As mentioned in Section 3.1, satellites grow according to the accretion timescale of Equation (19). Adding the exponential decay of the gas inflow, we can obtain the satellite mass as a function of time by integrating Equation (19):

$$\begin{aligned} \frac{M(t)}{10^{-4} M_P} &= \left[ 3.7 f_{d,in} \eta_{ice} \left( \frac{r}{20 R_P} \right)^2 \left( \frac{\tau_{dep}}{10^6 \text{ yrs}} \right) \right. \\ &\quad \times \left\{ 1 - \exp \left( \frac{-t}{\tau_{dep}} \right) \right\} \\ &\quad \times \left. + \left( \frac{M_0}{10^{-4} M_P} \right)^{2/3} \right]^{3/2}, \end{aligned} \quad (33)$$

where  $M_0$  is the initial mass. The time dependence of  $r$  is neglected. Figure 9 plots the mass of the largest three satellites as a function of  $f_{d,in}$  for 12 runs (models 1, 3-5). The circles, triangles, and squares express the mass at  $3 \times 10^5$ ,  $3 \times 10^6$ , and  $3 \times 10^7 T_K$ , respectively. The estimates of Equation (33) are also drawn with the dotted line ( $3 \times 10^5 T_K$ ), the dashed line ( $3 \times 10^6 T_K$ ), and the solid line ( $3 \times 10^7 T_K$ ), where  $r = 20 R_P$  is substituted. Because satellites migrate inward from the original locations, we neglect  $r$ -dependence. We find that the results are reasonably consistent with the estimates. However, it should be noted that although  $\Delta r = 10 r_H$  is assumed in deriving Equation (19), the orbital separation of satellites trapped by the edge can decrease to  $\lesssim 10 r_H$  with an increase in mass, and  $\Delta r$  becomes independent of  $M$ . Thus, the power-law index in the right-hand-side of Equation (33) decreases to unity. In fact, the slope at  $3 \times 10^7 T_K$  is close to the linear dependence of  $f_{d,in}$ .

Canup & Ward (2006) showed that the mass of satellites and the total mass in a system are both regulated by the balance between the supply of the inflowing materials and orbital decay due to type I migration. The critical mass is derived in Equation (20). However, in our case in which the inner cavity exists, the total mass regulation does not work effectively unless the eccentricity trap is inhibited. For a case in which the number of trapped satellites by the edge is equal to the critical number for the eccentricity trap, the configuration is destroyed and some satellites are lost to the planet if an additional satellite migrates and is trapped in a resonance. In other cases, the total mass continues to increase. As discussed in Sasaki et al. (2010), when the total mass of the trapped satellites exceeds the disk mass, the satellites may be released to the host planet, and mass regulation occurs. In addition, recent magnetohydrodynamic (MHD) simulations (e.g., Romanova et al. 2008) suggest that the inner cavity may be buried by intermittent gas accretion onto the planet, and satellites trapped by the

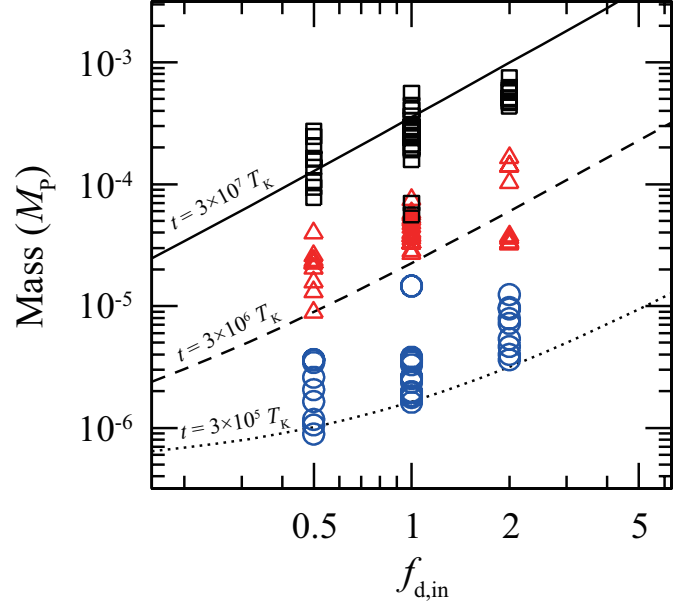


**Figure 9.** Mass of the largest three satellites at  $3 \times 10^5 T_K$  (blue circles),  $3 \times 10^6 T_K$  (red triangles), and  $3 \times 10^7 T_K$  (black squares) for models 1 and 3 ( $f_g = 1$ ), model 4 ( $f_g = 0.5$ ), and model 5 ( $f_g = 2$ ). The dotted, dashed, and solid lines are estimates of Equation (33) at  $3 \times 10^5 T_K$ ,  $3 \times 10^6 T_K$ , and  $3 \times 10^7 T_K$ , respectively.

edge would episodically fall. These effects should be examined in detail through MHD simulations.

With an analytical estimate of the growth timescale, model parameters can be constrained for the formation of the Galilean satellites. To prevent these parameters from exceeding the masses of the Galilean satellites,  $M_{crit} \leq 5 \times 10^{-5} M_P$  should be satisfied as a necessary condition, which leads to (Equation (20)):

$$\begin{aligned} \frac{\eta_{ice} f_{d,in}}{C_I f_g} &\leq 0.5 \left( \frac{M_P}{M_J} \right) \left( \frac{r}{20 R_P} \right)^{-5/2} \left( \frac{R_P}{R_J} \right)^{-1/2} \\ &\quad \times \left( \frac{\tau_G}{5 \times 10^6 \text{ yr}} \right)^{1/4}, \end{aligned} \quad (34)$$

where we neglect the impact erosion of ice. In addition, to be consistent with Callisto's partially differentiated state, an accretion time longer than  $\sim 5 \times 10^5$  years is implied to enable  $\eta_{ice} f_{d,in} < 1$  at the time of Callisto's accretion (Equation (19)).

#### 5. FORMATION OF SATURNIAN SYSTEM

Sasaki et al. (2010) proposed that Jupiter opened a gap in the protoplanetary disk to halt its growth, and Saturn did not. The circum-Saturnian disk gradually dissipated on the global depletion timescale of the protoplanetary disk; therefore, in the final stage of satellite accretion around Saturn, the circum-Saturnian disk did not have an inner cavity because a low accretion rate would lead to a weak magnetic field, as discussed in Section 2. This condition is comparable with that adopted in Canup & Ward (2006); however, properties of the Saturnian system are not commonly reproduced either by their  $N$ -body simulations or our preliminary  $N$ -body calculations without the inner cavity. That is, the average number of final satellites is  $\sim 3 - 4$ , while the number of large

satellites ( $\geq 10^{-5} M_P$ ) in the current Saturnian system is one (Titan). Hence, the solid material distribution produced by  $N$ -body calculations is also not consistent in the current Saturnian system.

According to Equation (19), the growth timescale of satellites decreases with distance from the central planet; therefore, satellite seeds predominantly develop in the outer region ( $\gtrsim 20 R_P$ ), and the satellites exhibit inward migration. If the migration rate significantly increases during migration, the migrating satellites rapidly fall onto the planet, and as a result, a single satellite always exists in Titan's orbit. Sasaki et al. (2010) assumed accelerated migration and showed that one or two satellites remain in the end; however, their method for generating satellite seeds is not appropriate for satellite formation. Because the migration timescale in protosatellite disks is proportional to  $r^{1/2}$  (Equation (12)), the migration rate is not accelerated ( $da/dt = a/t_a \simeq a^{1/2}$ ) during migration, which is observed in  $N$ -body simulations of Canup & Ward (2006) and in this study. It should be noted that planets in a minimum-mass nebula, in which a steeper surface density profile ( $\Sigma_g \propto r^{3/2}$ ) is considered, undergo accelerated migration, because  $t_a \propto r^{3/2}$ . Thus, we suggest in this section several possibilities to reconcile the inconsistency.

In our calculations and also in those of Canup & Ward (2006) and Sasaki et al. (2010), the radial dependence of the gas inflow is ignored, which results in a relatively gentle gradient of gas surface density ( $\Sigma_g \propto r^{-3/4}$ ). If the gas inflow flux is inversely proportional to  $r$  ( $F_{\text{in}} \propto r^{-\gamma}; \gamma > 0$ ), the gradient of gas surface density becomes steep; recent hydrodynamic simulations by Tanigawa et al. (2012) suggest that  $\gamma \sim 1$ . In addition, photoevaporation can produce the steep gradient of gas density (Mitchell & Stewart 2011). The type I migration speed increases in the region close to the central planet so that the satellites that begin to undergo migration are rapidly lost to the planet. Our preliminary  $N$ -body simulations that include this effect suggest that the number of satellites decreases with an increase in  $\gamma$ . More detailed calculations are required, and it is also important to examine the radial and time dependence of the inflow flux by a high-resolution hydrodynamic simulation.

Another possibility is that the solid density is locally increased around Titan's orbit ( $\simeq 20 R_P$ ), leading to the preferential growth of satellites in the region. The radial distribution of solid inflow and satellitesimal formation should be investigated. A detailed discussion of the Saturnian system formation will be presented in a separate paper.

## 6. CONCLUSIONS

We have investigated the formation of regular satellites around giant planets using direct  $N$ -body simulations, including the effects of the eccentricity trap near the disk edge and the damping of the semimajor axis and eccentricity. Through these simulations, we confirmed the following scenarios of the final stage of a satellite formation in a steady accretion disk with an inner cavity and a gas/solid inflow from a circumstellar disk:

1. Within the inflow region, protosatellites accrete from solid materials in their feeding zones. When

the satellites grow to the critical mass for migration, they begin to exhibit orbital decay. Because the width of the feeding zone increases with an increase in distance from the central planet and disk surface density has a relatively weak radial dependence ( $\Sigma_g \propto r^{-3/4}$ ), satellites in outer orbits grow larger than inner satellites.

2. When the satellites reach the inner disk edge, they cease inward migration. The subsequently migrating satellites are captured into mean motion resonances with the inner satellites. If the edge torque exerted on the innermost satellite balances the migration torque, the satellites are trapped near the edge, which is called as the eccentricity trap.
3. Satellites with the critical mass migrate inward to be trapped in successive resonances. If the number of trapped satellites exceeds the critical number for the eccentricity trap, the orbital configuration of the resonant convoy is disrupted, resulting in a loss of the inner satellites to the planet. That is, the total number of trapped satellites is self-regulated.
4. The disk gas of circumplanetary protosatellite disks quickly ( $\sim 10^3$  years) vanishes because of truncation of inflowing gas by the gap opening along the planet's orbit in the circumstellar disk, and resonant configuration is frozen at that time. Although the eccentricities of trapped satellites are excited by resonances, they are generally damped to  $\lesssim 0.01$  through long-term tidal dissipation within the satellites.

We tracked the compositional evolution of satellites in  $N$ -body simulations including the ice line beyond which water is condensed. As migration of icy satellites from the outer region ceases because of the eccentricity trap, inner satellites avoid contamination by water-rich materials, resulting in a radial compositional gradient. This composition is described as an increase in icy components with distance. In addition, it is suggested that to reproduce the compositional gradient, the gap opening needs to occur while the satellites are trapped by the edge via the eccentricity trap. An additional pathway for producing the compositional gradient is also suggested such that the volatile materials of inner satellites would be evaporated because of high-speed collisions during their accretion.

Furthermore, we examine the relationship between the characteristics of the final satellites and the model parameters by numerical simulations and semianalytical arguments to evaluate the probability of the Galilean-like satellite formation. The physical properties of the Galilean moons provide the following constraints on the model parameters. The number of satellites that can be trapped by the eccentricity trap restricts the ratio of the  $e$ -damping timescale versus the  $a$ -damping timescale:

$$\frac{t_e}{t_a} < 0.05, \quad (35)$$

where  $n = 3$  is substituted into Equation (24). Equation (35) is given as  $(c_s/v_K)^2 \lesssim 0.01/C_I$ , which is usually satisfied in the protosatellite disk with the temperature of Equation (5). The number of final satellites



also depends on the inflow region of the solid materials, although the actual inflow region of gas and dust for the circum-Jovian orbit is probably consistent with our adopted theory (Machida 2009). By considering capture into resonances, constraints on the  $e$ -damping and  $a$ -damping timescales are derived. A necessary condition for capture into the 2:1 resonance is

$$f_g < 700. \quad (36)$$

This parameter can be easily satisfied in the gas-starved disk ( $f_g = 1$ ), and this condition implies that an actively-supplied disk with either a much lower viscosity and/or a more rapid inflow rate than considered in previous works can also produce 2:1 resonant orbits. An additional condition for satellites with masses of  $5 \times 10^{-5} M_P$  is

$$C_I < 500 f_g^{-1}. \quad (37)$$

This parameter can also be satisfied because  $C_I \leq 1$ . We therefore find that formation of Galilean-like satellites is robust, because even with fast migration and a high gas surface density over three satellites, they are captured into the 2:1 mean motion resonance outside the disk inner edge. The parameters for growth and migration are also constrained by considering that the satellite mass does not exceed the critical mass for migration:

$$\frac{\eta_{ice} f_{d,in}}{C_I f_g} \leq 0.5. \quad (38)$$

It is also inferred that the solid inflow is decreased ( $\eta_{ice} f_{d,in} < 1$ ) at the time of Callisto's formation. In addition, to prevent Callisto from being captured into mean motion resonances, the gap opening timing of Jupiter should be comparable to the timing of the completion of Callisto formation. This theory is consistent not only with the gap opening time, which was inferred from the discussion of composition, but also with the time assumed in our calculation.

We finally provide theoretical predictions for characteristics of exomoons, which should be detected in the near future. If the disk inner edge width is sufficiently sharp, the eccentricity trap is likely to occur because the value of  $t_e/t_a$  is generally small even in the case that applies the full type I migration rate from the linear theory. The number of trapped satellites by the disk edge would be less than  $\sim 10$  because the inflow region of solid material is probably consistent with that in the adopted theory (Machida 2009). In the last stage of satellite accretion, the gas surface density would presumably be less than  $10^5 \text{ g cm}^{-2}$  so that the damping timescales of eccentricity and semimajor axis are sufficiently long to enable the capture of satellites into the 2:1 mean-motion resonance,

unless the mass of the satellite is significantly small.

These properties of multiple satellite formation and capture into resonances imply that the satellites can be substantially affected by tidal heating. The satellites that have a sufficient mass to retain water in the HZ are potentially habitable. Furthermore, according to tidal heating, their host planet is not required to be in the HZ; thus, the probability of forming Europa-like habitable satellites, which have tidally heated oceans, would be high. From the perspective of tidally heated habitable moons, it is probable that satellites in relatively outer orbits retain water compared to close-in moons, which are strongly heated. Tidal heating is extremely important for habitable moons; therefore, further study of the evolution of satellites including tidal heating is necessary. By considering the migration efficiency and the accretion rate, the mass of normal satellite size would be  $\sim 10^{-4} M_P$ , which is similar to that of the Galilean satellites and Titan. It is possible for observable exomoons ( $\gtrsim 0.2 M_\oplus \simeq 6 \times 10^{-4} M_J$ ) to form around giant planets more massive than Jupiter. Satellite systems with a large mass ratio of the satellite to the host planet are more stable for detecting exomoons (Kipping et al. 2012), and when the factor  $\eta_{ice} f_{d,in}/C_I f_g$  is larger than unity, larger satellites ( $\gtrsim 10^{-4} M_P$ ) are formed.

We find that several satellites are formed locked in resonances under the assumption that the host planet opens a gap around its orbit. Sasaki et al. (2010) proposed that if the planet does not create a gap, satellites are unlikely to form in resonances, such as that observed in Saturnian satellites. Because a gap opening indicates that the planet may undergo type II migration, it is expected that satellites systems in mean motion resonances migrate inward to some extent. Therefore, planets that reside in closer orbits probably harbor Jovian-system-like moons, although destabilization by tidal torque (Barnes & O'Brien 2002) or shrinkage of Hill sphere (Namouni 2010) may also be important. In contrast, Saturnian-system-like moons orbit more distant planets.

## ACKNOWLEDGMENT

We thank the anonymous referee for useful comments that improved and clarified this manuscript. We also thank Francis Nimmo and Takanori Sasaki for their fruitful discussion and valuable suggestions. Numerical computations were in part conducted on GRAPE system and the general-purpose PC farm at Center for Computational Astrophysics, CfCA, of National Astronomical Observatory of Japan. This work is supported by Grant-in-Aid for JSPS Fellows (23004841).

## APPENDIX

### ACTIVELY SUPPLIED DISK MODEL

On the basis of Canup & Ward (2002), the asymptotic disk gas surface density for a steady accretion disk is given by

$$\Sigma_g \simeq \frac{F_P}{3\pi\nu} \left[ 1 - \frac{4}{5} \sqrt{\frac{r_c}{r_d}} - \frac{1}{5} \left( \frac{r}{r_c} \right)^2 \right] \simeq 0.55 \frac{F_P}{3\pi\nu}, \quad (A1)$$

where  $r_d$  is the outer edge of the diffused-out disk. The second and third terms in the bracket are correction terms due to outward diffusion.

The disk is heated by luminosity from the central planet, viscous dissipation, and energy dissipation associated with

the difference between the free-fall energies of the incoming gas and a Keplerian orbit. We assume that heating is dominated by viscous dissipation; then, the photospheric temperature of the disk ( $T_d$ ) is determined by a balance between viscous heating and blackbody radiation from the photosphere:

$$\sigma_{\text{SB}} T_d^4 \simeq \frac{9}{8} \Omega \nu \Sigma_g \simeq \frac{0.55 \times 3}{8\pi} \Omega^2 F_P \quad (\text{A2})$$

where  $\sigma_{\text{SB}}$  is the Stephan-Boltzman constant. When  $F_P = M_P/\tau_G$ , the temperature is reduced to

$$T_d \simeq 160 \left( \frac{M_P}{M_J} \right)^{1/2} \left( \frac{\tau_G}{5 \times 10^6 \text{ yr}} \right)^{-1/4} \left( \frac{r}{20 R_P} \right)^{-3/4} \left( \frac{R_P}{R_J} \right)^{-3/4} \text{ K}. \quad (\text{A3})$$

The midplane temperature  $T$  is approximately given by  $T \simeq (1 + 3\tau/8)^{1/4} T_d$ , where  $\tau$  is the optical depth. Because we are concerned with the disk temperature for evolution of the ice line, we assume that  $T \simeq T_d$  to avoid uncertainty in opacity.

Thus, by adopting the alpha model for disk viscosity ( $\nu = \alpha c_s H$ ), the gas surface density of the disk becomes

$$\Sigma_g \simeq 0.55 \frac{F_P}{3\pi\nu} \simeq 100 f_g \left( \frac{M_P}{M_J} \right) \left( \frac{r}{20 R_P} \right)^{-3/4} \left( \frac{R_P}{R_J} \right)^{-3/4} \text{ g cm}^{-2}, \quad (\text{A4})$$

$$f_g \equiv \left( \frac{\alpha}{5 \times 10^{-3}} \right)^{-1} \left( \frac{\tau_G}{5 \times 10^6 \text{ yr}} \right)^{-3/4}. \quad (\text{A5})$$

#### GROWTH TIMESCALE

The growth rate of satellites is determined by the velocity dispersion  $\sigma$  and the spatial density of satellitesimals  $\rho_d$ . When velocity dispersion is smaller than the surface escape velocity of the satellite core, the accretion rate of the core with the mass  $M$  at  $r$  is

$$\dot{M} \simeq \pi C R^2 \rho_d \left( \frac{2GM}{R\sigma^2} \right) \sigma \simeq \pi C R^2 \Sigma_d \Omega_K \left( \frac{2GM}{R\sigma^2} \right) \left( = 2\pi C \left( \frac{R}{r} \right) \left( \frac{\Sigma_d r^2}{M_P} \right) \left( \frac{v_K}{\sigma} \right)^2 M \Omega_K \right), \quad (\text{B1})$$

where  $C$  is a numerical factor of 2-3 (Stewart & Ida 2000) and  $\Sigma_d$  is the surface density of satellitesimals in the disk. Because  $R/r$  and  $\Sigma_d r^2/M_P$  are large compared to the corresponding values for planetary growth at  $\sim 1$  AU around the Sun, the accretion rate is relatively high. Thus, the accretion timescale is

$$\tau_{\text{acc,core}} = \frac{M}{\dot{M}} \quad (\text{B2})$$

$$\begin{aligned} &\simeq 3 \times 10^3 \left( \frac{C}{2.5} \right)^{-1} \left( \frac{\Sigma_d}{50 \text{ g cm}^{-2}} \right)^{-1} \left( \frac{\rho}{3 \text{ g cm}^{-3}} \right)^{1/3} \left( \frac{M}{10^{-4} M_P} \right)^{-1/3} \left( \frac{M_P}{M_J} \right)^{1/6} \\ &\times \left( \frac{r}{20 R_P} \right)^{1/2} \left( \frac{R_P}{R_J} \right)^{1/2} \left( \frac{e}{0.1} \right)^2 \text{ yr}, \end{aligned} \quad (\text{B3})$$

where  $\rho$  and  $e$  are the internal density of the core and the RMS eccentricity of satellitesimals, respectively. Through numerical simulations, we find that  $\Sigma_d \sim 50 \text{ g cm}^{-2}$  and  $e \sim 0.1$ .

However, in the case in which the core accretion timescale  $\tau_{\text{acc,core}}$  is smaller than the mass inflow timescale  $\tau_{\text{acc,inflow}}$ , the growth timescale is controlled by the inflow flux of solid materials, as determined by Canup & Ward (2006). Satellites accrete materials across an annulus of width  $\Delta r$  and grow in the timescale as

$$\tau_{\text{acc,inflow}} = \frac{M}{\dot{M}} \simeq \frac{fM}{F_{\text{in}} 2\pi r \Delta r} \quad (\text{B4})$$

$$\simeq 1.8 \times 10^5 \eta_{\text{ice}}^{-1} f_{\text{d,in}}^{-1} \left( \frac{r}{20 R_P} \right)^{-2} \left( \frac{M}{10^{-4} M_P} \right)^{2/3} \text{ yr}, \quad (\text{B5})$$

where  $f (= 100/\eta_{\text{ice}} f_{\text{d,in}})$  is the gas-to-solid mass ratio in the inflow, and  $\Delta r = 10 r_H$  is used. This derivation differs slightly from that of Canup & Ward (2006), in which  $\Delta r \sim 2er$  is assumed. However, the timescale is approximately consistent. Obviously,  $\tau_{\text{acc,inflow}}$  is longer than  $\tau_{\text{acc,core}}$ ; thus,  $\tau_{\text{acc,inflow}}$  can be considered as the growth timescale of the satellite. These estimates are in good agreement with numerical results shown in the text.

#### RESONANT ANGLE

The angels are defined as

$$\theta_1 = \lambda_1 - 2\lambda_2 + \varpi_1, \quad (\text{C1})$$

$$\theta_2 = \lambda_1 - 2\lambda_2 + \varpi_2, \quad (\text{C2})$$

$$\theta_3 = \lambda_2 - 2\lambda_3 + \varpi_2, \quad (\text{C3})$$

$$\theta_4 = \lambda_2 - 2\lambda_3 + \varpi_3, \quad (\text{C4})$$

$$\theta_5 = \theta_2 - \theta_3 = \lambda_1 - 3\lambda_2 + 2\lambda_3, \quad (\text{C5})$$

where  $\lambda_i$  and  $\varpi_i$  are mean orbital longitudes and longitudes of the pericenter, respectively. The subscripts  $i = 1, 2$ , and  $3$  refer to the innermost satellite (body 1), the second satellite (body 2), and the third satellite (body 3), respectively. These angles represent displacements of longitude of conjunction from pericenters; thus,  $\theta_1 = 0^\circ$ ,  $\theta_2 = 180^\circ$  indicates that conjunctions of body 1 and body 2 occur when body 1 is near the apocenter and body 2 is near the pericenter. If the angles librate about some fixed values, it is usually considered that they are in mean motion resonances. In addition, the Laplace resonance is characterized by the libration of  $\theta_5$ . In this case, conjunctions of body 1 and body 2 drift at the same rate as those of body 2 and body 3 so that triple conjunction is impossible.

For the Galilean satellites,  $\theta_1$  and  $\theta_2$  librate about  $0^\circ$  and  $180^\circ$ , respectively, indicating that the conjunction longitude between Io and Europa is locked to Io's pericenter and Europa's apocenter.  $\theta_3$  librates about  $0^\circ$ , while  $\theta_4$  circulates through  $360^\circ$ , which indicates that the Europa-Ganymede conjunction is locked to Europa's pericenter but to neither apse of Ganymede. Thus,  $\theta_5$  obviously librates about  $180^\circ$ , indicating a Laplace relationship.

## REFERENCES

- Anderson, J. D., Jacobson, R. A., McElrath, T. P., Moore, W. B., Schubert, G., & Thomas, P. C. 2001, *Icarus*, 153, 157
- Artymowicz, P. 1993, *ApJ*, 419, 166
- Barnes, J. W., & O'Brien, D. P. 2002, *ApJ*, 575, 1087
- Barr, A. C., & Canup, R. M. 2008, *Icarus*, 198, 163
- Binney, J., & Tremaine, S. 1987, *Nature*, 326, 219
- Bouchy, F., Mayor, M., Lovis, C., Udry, S., Benz, W., Bertaux, J. -L., Delfosse, X., Mordasini, C., Pepe, F., Queloz, D., & Segransan, D. 2009, *A&A*, 496, 527
- Canup, R. M., & Ward, W. R. 2002, *ApJ*, 124, 3404
- Canup, R. M., & Ward, W. R. 2006, *Nature*, 441, 834
- Canup, R. M., & Ward, W. R. 2009, in *Europa*, ed. R. T. Pappalardo, W. B. McKinnon, & K. Khurana (Tuscon: Univ. Arizona Press), 59
- Eisner, J. A., Hillenbrand, L. A., White, R. J., Akeson, R. L., & Sargent, A. I. 2005 *ApJ*, 623, 952
- Estrada, P. R., Mosqueira, I., Lissauer, J. J., D'Angelo, G., & Cruikshank, D. P. 2009, in *Europa*, ed. R. T. Pappalardo, W. B. McKinnon, & K. Khurana (Tuscon: Univ. Arizona Press), 27
- Friedland, L. 2001, *ApJ*, 547, L45
- Fujii, Y. I., Okuzumi, S., & Inutsuka, S. 2011, *ApJ*, 743, 53
- Goldreich, P., & Soter, S. 1966, *Icarus*, 5, 375
- Goldreich, P., & Tremaine, S. 1980, *ApJ*, 241, 425
- Greenberg, R. 1987, *Icarus*, 70, 334
- Hartmann, L. 2002, *ApJ*, 566, L29
- Hasegawa, M. & Nakazawa, K. 1990, *A&A*, 227, 619
- Hayashi, C. 1981, *Prog. Theor. Phys. Suppl.*, 70, 35
- Herbst, W., & Mundt, R. 2005, *ApJ*, 633, 967
- Ida, S., Bryden, G., Lin, D. N. C., & Tanaka, H. 2000, *ApJ*, 534, 428
- Ida, S., & Lin, D. N. C. 2004, *ApJ*, 604, 388
- Ida, S. & Lin, D. N. C. 2008, *ApJ*, 673, 484
- Ida, S. & Lin, D. N. C. 2010, *ApJ*, 719, 810
- Ida, S., & Makino, J. 1992, *Icarus*, 96, 107
- Kaltenegger, L. 2000, in *Proc. Exploration and Utilisation of the Moon: ICEUM 4*, ed. B. H. Foing & M. Perry (ESA SP-462; Noordwijk: ESA), 199
- Kaltenegger, L. 2010, *ApJ*, 712, L125
- Kasting, J. F., Whitmire, D. P., & Reynolds, R. T. 1993, *Icarus*, 101, 108
- Kipping, D. M., Fossey, S. J., & Campanella, G. 2009, *MNRAS*, 400, 398
- Kipping, D. M., Bakos, G. Á., Buchhave, L., Nesvorný, D., & Schmitt, A. 2012, *ApJ*, submitted
- Kokubo, E. & Ida, S. 1998, *Icarus*, 131, 171
- Kraus, R. G., Senft, L. G., & Stewart, S. S. 2011, *Icarus*, 214, 724
- Lin, D. N. C., & Papaloizou, J. C. B. 1985, in *Protostars and Planets II*, ed. D. C. Black & M. S. Matthews (Tuscon: Univ. Arizona Press), 981
- Lo Curto, G., Mayor, M., Benz, W., Bouchy, F., Lovis, C., Moutou, C., Naef, D., Pepe, F., Queloz, D., Santos, N. C., Segransan, D., & Udry, S. 2010, *A&A*, 512, A48
- Lubow, S. H., Seibert, M., & Artymowicz, P. 1999, *ApJ*, 526, 1001
- Lunine, J. I., & Stevenson, D. J. 1982, *Icarus*, 52, 14
- Lyra, W., Paardekooper, S. -J., & Mac Low, M. -M. 2010 *ApJ*, 715, L68
- Machida, M. 2009 *MNRAS*, 392, 514
- Makino, J. 1991, *ApJ*, 369, 200
- Makinio, J., & Aarseth, S. J. 1992, *PASJ*, 44, 141
- Masset, F. S., D'Angelo, G., & Kley, W. 2006, *ApJ*, 652, 730
- Mayor, M., Udry, S., Lovis, C., Pepe, F., Queloz, D., Benz, W., Bertaux, J. -L., Bouchy, F., Mordasini, C., & Segransan, D. 2009, *A&A*, 493, 636
- Mitchell, T. R., & Stewart, G. R. 2011, *AJ*, 142, 168
- Mosqueira, I., & Estrada, P. R. 2003, *Icarus*, 163, 198
- Mosqueira, I., & Estrada, P. R. 2003, *Icarus*, 163, 232
- Murray, C. D., & Dermott, S. F. 1999, *Solar System Dynamics* (Cambridge: Cambridge Univ. Press)
- Mustill, A. J., & Wyatt, M. C. 2011, *MNRAS*, 413, 554
- Muto, T., Takeuchi, T., & Ida, S. 2011, *ApJ*, 737, 37
- Nakazawa, K., & Ida, S. 1988, *Prog. Theor. Phys. Suppl.*, 96, 167
- Namouni, F. 2010, *ApJ*, 719, L145
- Nimmo, F., & Korycansky, D. G. 2012, *Icarus*, in press.
- Ogihara, M., & Ida, S. 2009, *ApJ*, 699, 824
- Ogihara, M., Duncan, M. J., & Ida, S. 2010, *ApJ*, 721, 1184
- Ostriker, E. C. 1999, *ApJ*, 513, 252
- Paardekooper, S. -J., Baruteau, C., Crida, A., & Kley, W. 2010 *MNRAS*, 401, 1950
- Papaloizou, J. C. B., & Larwood, J. D. 2000 *MNRAS*, 315, 823
- Papaloizou, J. C. B., & Terquem, C. 2010, *MNRAS*, 405, 573
- Peale, S. J., & Lee, M. H. 2002, *Science*, 298, 593
- Quillen, A. C. 2006, *MNRAS*, 365, 1367
- Romanova, M. R., Kulkarni, A. K., and Lovelace, R. V. E. 2008 *ApJ*, 673, L171
- Shakura, N. I., & Sunyaev, R. A. 1973, *A&A*, 24, 337
- Sasaki, T., Ida, S., & Stewart, G. R. 2010, *ApJ*, 714, 1052
- Saumon, D., & Guillot, T. 2004, *ApJ*, 609, 1170
- Seidelmann, K. P., ed. 1992, *Explanatory Supplement to the Astronomical Almanac* (Sausalito: University Science Books)
- Schubert, G., Anderson, J. D., Spohn, T., & McKinnon, W. B. 2004, in *Jupiter: The Planet, Satellites and Magnetosphere*, ed. F. Bagenal, T. E. Dowling, & W. B. McKinnon (Cambridge: Cambridge Univ. Press), 281
- Stewart, G. R., & Ida, S. 2000, *Icarus*, 143, 28
- Takata, T., & Stevenson, D. J. 1996, *Icarus*, 123, 404

- Tanaka, H., Takeuchi, T., & Ward, W. R. 2002, *ApJ*, 565, 1257
- Tanaka, H., & Ward, W. R. 2004, *ApJ*, 602, 388
- Tanigawa, T., Ohtsuki, K., & Machida, M. 2012, *ApJ*, in press.
- Terquem, C., & Papaloizou, J. C. B. 2007, *ApJ*, 654, 1110
- Ward, W. R. 1986, *Icarus*, 67, 164
- Ward, W. R. 1988, *Icarus*, 73, 330
- Ward, W. R., & Canup, R. M. 2010, *AJ*, 140, 1168
- Williams, D. M., Kasting, J. F., & Wade, R. A. 1997, *Nature*, 385, 234
- Wyatt, M. C. 2003 *ApJ*, 598, 1321
- Yoder, C. F. 1979, *Nature*, 279, 767
- Yoder, C. F. 1995, in *Global Earth Physics, A Handbook of Physical Constants*, ed. T. Ahrens (Washington, DC: AGU), 1
- Yoder, C. F., & Pealse, S. J. 1981 *Icarus*, 47, 1